

614418

**NASA SUN-EARTH CONNECTIONS THEORY PROGRAM
CONTRACT NAS5-99188**

The Structure and Dynamics of the Solar Corona
and Inner Heliosphere

FIRST QUARTER SECOND YEAR PROGRESS REPORT
Covering the period August 16, 2000 to December 15, 2000



**NASA SUN-EARTH CONNECTIONS THEORY PROGRAM
CONTRACT NAS5-99188**

The Structure and Dynamics of the Solar Corona
and Inner Heliosphere

FIRST QUARTER SECOND YEAR PROGRESS REPORT
Covering the period August 16, 2000 to December 15, 2000

Submitted by:

Zoran Mikić
Principal Investigator
Science Applications International Corporation
10260 Campus Point Drive
San Diego, CA 92121

January 18, 2001

FIRST QUARTER SECOND YEAR PROGRESS REPORT

This report covers technical progress during the first quarter of the second year of NASA Sun-Earth Connections Theory Program (SECTP) contract "The Structure and Dynamics of the Solar Corona and Inner Heliosphere," NAS5-99188, between NASA and Science Applications International Corporation, and covers the period August 16, 2000 to December 15, 2000. Under this contract SAIC and the University of California, Irvine (UCI) have conducted research into theoretical modeling of active regions, the solar corona, and the inner heliosphere, using the MHD model.

The renewal of Option 2 of this contract (which renewed Year 2 of the contract from 8/16/2000 until 8/15/2001), was delayed due to contracting delays at NASA. The renewal was not received until November 27, 2000. As a consequence, the progress reported in this "quarterly" report includes a four-month period, rather than the customary three-month period. The actual funded time period during this time was from November 27, 2000 to December 15, 2000.

In the following sections we summarize our progress during this reporting period. Full descriptions of our work can be found in the cited publications, a few of which are attached to this report.

Publication on the Magnetic Field Topology in Prominences

The paper "Magnetic Field Topology and Modeling of Loops in Prominences," by R. Lionello, Z. Mikić, J. A. Linker, and T. Amari, has been submitted for publication in *The Astrophysical Journal Letters*. We present a computational model of the magnetic field lines in a prominence. We describe how the process of flux dispersal and cancellation in a realistic configuration can lead to the formation of a stable flux rope structure. The flux rope fulfills several theoretical and observational constraints associated with prominences: twist, shear along the neutral line, and dips. We have performed 1D hydrodynamic simulations along selected field lines in the final state to show that the flux rope can support cold and dense material that is characteristic of a prominence. The referee's comments have been received, and the paper is currently being revised for resubmission. This paper is included in Appendix A.

Publication on an Empirically-Driven Global MHD Model of the Solar Corona and Inner Heliosphere

The paper "An Empirically-Driven Global MHD Model of the Solar Corona and Inner Heliosphere," by P. Riley, J. A. Linker, and Z. Mikić, has been submitted for publication in *Journal of Geophysical Research*. We have developed a three-dimensional MHD model of the solar corona and heliosphere. We split the modeling region into two distinct parts: the solar corona (1 solar radius, R_s , to $30 R_s$) and the inner heliosphere ($30 R_s$ to 5 AU). This combined model is driven solely by the observed line-of-sight photospheric magnetic field and can thus provide a realistic global picture of the corona and heliosphere for specific time periods of

REPORT DOCUMENTATION PAGE

Form Approved
OMB No. 0704-0188

Public reporting burden for this collection of information is estimated to average 1 hour per response, including the time for reviewing instructions, searching existing data sources, gathering and maintaining the data needed, and completing and reviewing the collection of information. Send comments regarding this burden estimate or any other aspect of this collection of information, including suggestions for reducing this burden, to Washington Headquarters Services, Directorate for Information Operations and Reports, 1215 Jefferson Davis Highway, Suite 1204, Arlington, VA 22202-4302, and to the Office of Management and Budget, Paperwork Reduction Project (0704-0188), Washington, DC 20506.

1. AGENCY USE ONLY (Leave Blank)

2. REPORT DATE
January 18, 2001

3. REPORT TYPE AND DATES COVERED
2nd Year 1st Quarter Progress Report
08/16/00-12/15/00

4. TITLE AND SUBTITLE

The Structure and Dynamics of the Solar Corona and Inner Heliosphere:
2nd Year 1st Quarter Progress Report

5. FUNDING NUMBERS
NAS5-99188

6. AUTHORS

Zoran Mikic

7. PERFORMING ORGANIZATION NAME(S) AND ADDRESS(ES)

Science Applications International Corporation
10260 Campus Point Drive
San Diego, CA 92121-1578

8. PERFORMING ORGANIZATION
REPORT NUMBER
SAIC-00/8032:APPAT-265
01-0157-04-2065-000

9. SPONSORING/MONITORING AGENCY NAME(S) AND ADDRESS(ES)

NASA Headquarters Operation Office
Goddard Space Flight Center
Greenbelt, MD 20771

10. SPONSORING/MONITORING AGENCY
REPORT NUMBER

11. SUPPLEMENTARY NOTES

12a. DISTRIBUTION/AVAILABILITY STATEMENT

12b. DISTRIBUTION CODE

13. ABSTRACT (Maximum 200 words)

This report details progress during the first quarter of the second year of the Sun-Earth Connections Theory Program contract, "The Structure and Dynamics of the Solar Corona and Inner Heliosphere."

14. SUBJECT TERMS

Solar Corona, Coronal Magnetic Field, Heliosphere, Magnetohydrodynamics

15. NUMBER OF PAGES

49

16. PRICE CODE

17. SECURITY CLASSIFICATION
OF REPORT

UNCLASSIFIED

18. SECURITY CLASSIFICATION
OF THIS PAGE

UNCLASSIFIED

19. SECURITY CLASSIFICATION
OF ABSTRACT

UNCLASSIFIED

20. LIMITATION OF ABSTRACT

UL

interest. We have used the model to illustrate heliospheric structure during three different phases of the solar cycle: (1) Carrington Rotation (CR) 1913 (August 22, 1996–September 18, 1996), which occurred near solar minimum and overlapped the “Whole Sun Month” campaign; (2) CR 1892 (January 27, 1995–February 23, 1995), which occurred during the declining phase of cycle 22 and coincided with the so-called “Ulysses rapid latitude scan”; and (3) CR 1947 (March 7, 1999–April 4, 1999), which occurred approximately 15 months before the predicted maximum of solar cycle 23. We compared Ulysses and WIND observations with the simulation for CR1913 and compared Ulysses observations during its traversal from pole to pole with CR1892. We found that the simulations reproduce the overall large-scale features of the observations. Using the near solar maximum results, we have speculated on the structure of the high-latitude solar wind that Ulysses will encounter during its traversal of the southern and northern solar poles in 2000 and 2001, respectively. In particular, the results suggested that, due to the presence of equatorial coronal holes, the ordered pattern of CIR tilts and their associated shocks, which was observed during Ulysses initial southward excursion in 1992, will likely disappear completely as Ulysses moves toward the south pole. We anticipate that Ulysses will encounter fast streams but will not remain within them for more than a fraction of a solar rotation. Finally, the simulations suggested that crossings of the HCS will persist up to at least $\sim 70^\circ$ heliographic latitude. The paper has been revised, based on the referee’s comments, and has been accepted for publication. This paper is included in Appendix B.

Publication on Self-Consistent Formation of Prominences

The paper “Magnetohydrodynamic Modeling of Prominence Formation Within a Helmet Streamer,” by J. A. Linker, R. Lionello, Z. Mikić, and T. Amari, has been submitted for publication in *Journal of Geophysical Research*. This paper describes the self-consistent simulation of the formation of prominences in the solar corona. We present a 2D axisymmetric MHD model to self-consistently describe the formation of a stable prominence that supports cool, dense material in the lower corona. The upper chromosphere and transition region are included in the calculation. The prominence is formed by shearing a coronal arcade and reducing the magnetic flux, to form a magnetic field configuration with a flux-rope topology. The prominence forms when dense chromospheric material is brought up and condenses in the corona. The prominence sits at the base of a helmet streamer structure. The dense material is supported against gravity in the dips of the magnetic field lines in the flux rope. Further reduction in magnetic flux leads to an eruption of the prominence, ejecting material into the solar wind. The paper has been revised, based on the referee’s comments, and has been accepted for publication. A copy of this paper is included in Appendix C.

Eruption of a Magnetic Field Arcade by Flux Eruption/Cancellation

It is well documented that strongly sheared magnetic fields observed on the photosphere are often associated with solar activity, some of which results in violent energy release in the form of coronal mass ejections and solar flares. The modeling of these events involves: (a) the buildup of the sheared field, (b) the triggering of the release of free energy, and (c) the

subsequent dynamical events, including energetic plasma motions. We have demonstrated the energy buildup and release mechanisms by following the dynamic evolution of a magnetic arcade using 3-D numerical simulation.

The sheared magnetic-field structures in the solar atmosphere can be dynamically formed in two fundamentally different ways as shown in our previous investigations. A current-carrying magnetic loop, for example, can be formed by plasma flows on the photosphere with an initially potential field (Van Hoven *et al.* 1995). The fluid motions induce an electric current by twisting the in situ field lines. Alternatively, a current-carrying loop can emerge directly from underneath the photosphere by breaking through the surface (Mok *et al.* 1997). The end results are remarkably similar, provided the physical parameters are comparable. In the present effort, we chose to build up the sheared magnetic structure by prescribing plasma flows on the surface at the location where there is initially a potential magnetic arcade field. The flow pattern, in general, can be arbitrary on the solar surface. However, we have identified two parameter regimes that lead to fundamentally different consequences in our dynamic model. In the first case, in which the spatial scale of the flow around the magnetic neutral line is small compared to the spatial scale of the field, free magnetic energy is built up, and stored, primarily in a small region along the neutral line. In the second case, the flows and the field have comparable spatial scales everywhere, and free magnetic energy is built up throughout the structure. The triggering mechanism to release the magnetic energy in our model is the emergence of a new, potential arcade field with polarity opposite to the original arcade. This process essentially weakens, and disrupts, the potential component of the sheared field structure. Since the plasma flows in the buildup phase are very slow compared to the Alfvén speed, the sheared arcade is near force-free MHD equilibrium. The disruption of the potential component could trigger an analog of the ideal MHD kink instability, one of the most unstable modes often seen in laboratory devices.

In the first parameter regime, we began with two elongated, parallel magnetic poles of opposite polarity as a potential field structure. A flux-preserving, sheared flow is applied to the surface in such a way that the flow is highly concentrated along the magnetic neutral line with a spatial scale much smaller than the dimension of the magnetic poles. The maximum flow speed at the base is 0.01 of the Alfvén velocity, and this buildup phase lasts 190 Alfvén transit times. At the end of this period, when the flows stop, free magnetic energy is built up primarily along the neutral line at a relatively low altitude in a highly localized manner. After the buildup, a new bipole with polarities opposite to the original is slowly emerged from the surface on a time scale of 100 Alfvén times. The dynamic evolution is shown in Figure 1. At $t = 50$ (measured after the beginning of the new flux emergence), the magnetic structure continues to rise slowly into the corona. Some of the field lines become helical as a result of reconnection between the new flux and the existing, strongly sheared flux, whose field lines are nearly parallel to the neutral line. The instability is triggered at approximately $t = 80$, when the strength of the new flux passes a threshold. The structure suddenly explodes upward on an ideal MHD time scale. The similarity of this eruptive behavior with the MHD kink instability is quite evident. By $t = 87$, the end of this simulation, the flux is being ejected out of the corona at a speed exceeding 0.4

times the Alfvén velocity. This case is extremely dynamic. We believe that this is a plausible model for impulsive events such as coronal mass ejections and solar flares.

In the second parameter regime, we applied a surface flow to the same bipole region to build up magnetic energy. The plasma flows, however, follow the contours of the vertical component of the magnetic field so that the field lines of the entire region are evenly subjected to the twisting motions. Free magnetic energy is built up throughout the structure, which expands slowly into the corona during the process. We were able to store more free energy in the system at the same value of resistivity, which eventually limits the growth of the electric current density. However, when the shearing stops and new flux is emerged, as in the last case, a magnetic tearing mode is excited on the vertical current sheet directly above the neutral line, resulting in an upward-downward flow pattern away from the X-point. The speed is typically a few percent of the Alfvén velocity, and the evolution is on a slower time scale than in the previous case. This event is not explosive, and might correspond to the small plasma flows observed in some prominences.

A preliminary version of this work was presented in the paper "Effects on Magnetic Structures by Disrupting Plasma Flows and Surface Magnetic Fields," by Y. Mok, J. A. Linker, and Z. Mikić, at the meeting of the American Astronomical Society/Solar Physics Division, held in Lake Tahoe, Nevada, June 18–22, 2000. These results are currently being prepared for publication.

REFERENCES

- Van Hoven, G., Mok, Y., & Mikić, Z. 1995, *Ap. J.*, **440**, L105.
Mok, Y., Van Hoven, G., & Mikić, Z. 1997, *Ap. J.*, **490**, L107.

Eruption of an Arcade Caused by Flux Emergence

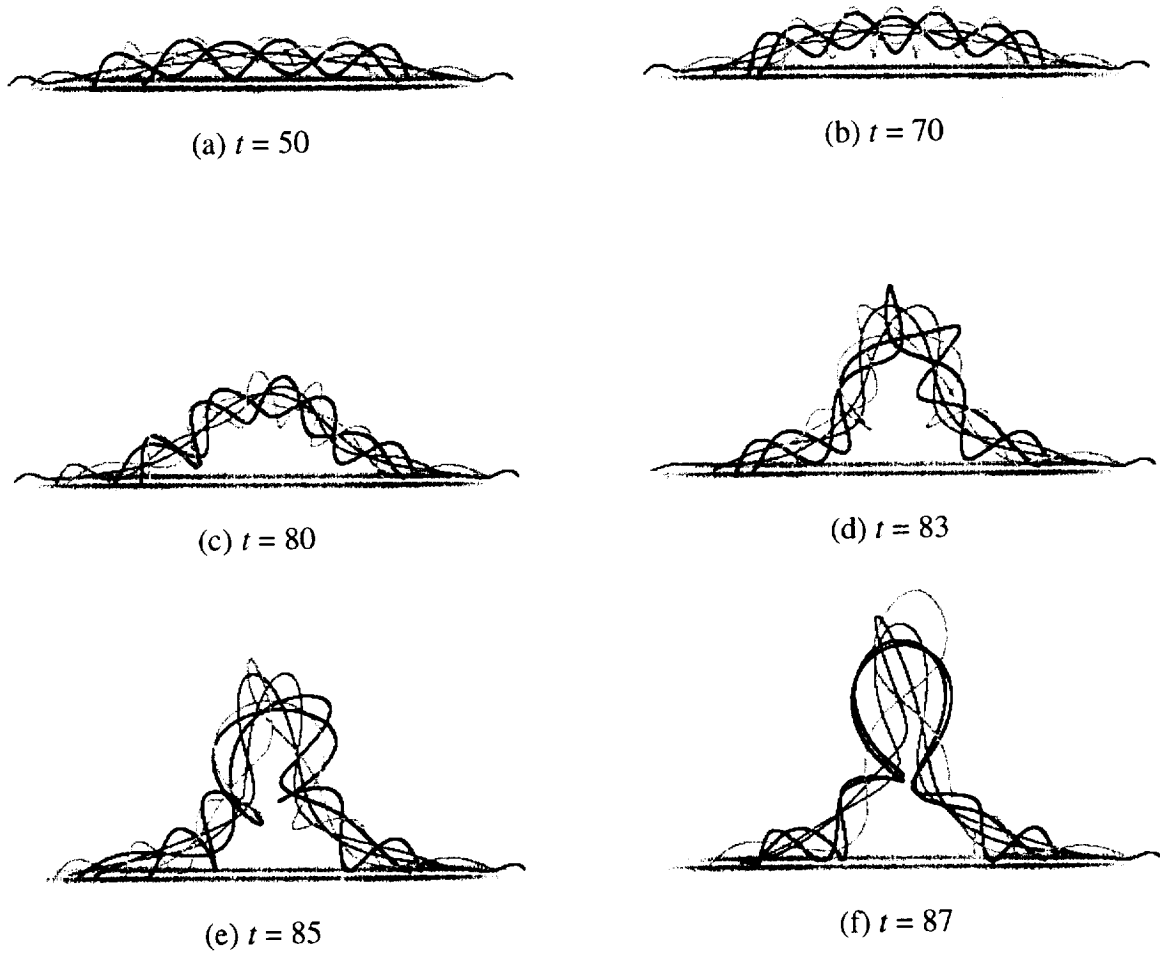


Figure 1. A time sequence showing the dynamic evolution of the magnetic field lines of a highly sheared bipole region when new flux of opposite polarity emerges from underneath the photosphere. The new flux begins to emerge at $t = 0$. The sequence corresponds to (a) $t = 50$, (b) $t = 70$, (c) $t = 80$, (d) $t = 83$, (e) $t = 85$ and (f) $t = 87$. The simulation was run on a mesh of $127 \times 79 \times 71$ points in (x, y, z) , with a Lundquist number of $S = 5 \times 10^4$. The field lines in all six frames are traced from the same set of footpoints at the base.

APPENDIX A

“Magnetic Field Topology and Modeling of Loops in Prominences”

R. Lionello, Z. Mikić, J. A. Linker, and T. Amari

Submitted for publication in *The Astrophysical Journal Letters*

Magnetic Field Topology and Modeling of Loops in Prominences

Roberto Lionello, Zoran Mikić, Jon A. Linker,

Science Applications International Corporation, San Diego, CA 92121-1578

{lionel,mikic,linker}@iris023.saic.com

and

Tahar Amari

Centre de Physique Théorique, École Polytechnique, 91128 Palaiseau Cedex, France

amari@cpht.polytechnique.fr

Received _____: accepted _____

ABSTRACT

We present a computational model of the magnetic field lines in a prominence. We show how the process of flux dispersal and cancellation in a realistic configuration can lead to the formation of a stable flux rope structure. The flux rope fulfills several theoretical and observational constraints associated with prominences: twist, shear along the neutral line, and dips. We perform 1D hydrodynamic simulations along selected field lines in the final state to show that the flux rope can support cold and dense material that is characteristic of a prominence.

Subject headings: MHD -- Sun: corona -- Sun: magnetic fields --
Sun: prominences

1. Introduction

Prominences are formed of material that is hundreds of times cooler and denser than the surrounding corona. They are often observed to lie along the neutral line separating regions of opposite polarity (Priest 1982). Considerable research has been performed in the past in order to find a favorable background magnetic configuration to support prominences against gravity (Priest 1982). One possibility is to start from a field generated by a dipole and apply a shear flow concentrated along the neutral line, which results in an equilibrium with dipped field lines (Antiochos et al. 1994). The presence of localized heating near the chromosphere makes it possible to form condensations, whose collective appearance is the prominence (Dahlburg et al. 1998; Antiochos et al. 1999).

Our approach is driven by different theoretical considerations, which indicate that a flux rope is a viable candidate to support the denser and cooler prominence material. A

flux rope fulfills several of the theoretical and observational requirements such as twist, shear along the neutral line, and dips [however there are also observations that suggest the presence of vertical magnetic field in apparent contrast to this model (Zircher et al. 1998)]. Amari et al. (1999) have shown how flux dispersal and cancellation in an idealized sheared arcade field can lead to the formation of a stable flux rope structure. In this work we show how a similar process leads to the formation of a stable flux rope and we study the condensation of plasma along the loop's magnetic field lines in this topology. For our model we are motivated by observations of a prominence seen on September 23, 1996 (see Fig. 1). The final configuration consists of a twisted magnetic flux tube embedded in an overlying, almost potential, arcade. We then solve the 1D hydrodynamic equations along the field lines in this final state in order to show that the flux rope can support the cold and dense material that is characteristic of a prominence. Our work does not directly address how condensations are actually created. One possibility is that formation occurs by lifting of chromospheric material during the dispersal and cancellation phase. Siphon flows represent another possible mechanism (Antiochos et al. 1999)

2. The MHD Model and Simulations

Our approach is based on two separate models. We use a 3D MHD model to obtain the magnetic structure. Then we solve the 1D hydrodynamic equations along field lines to obtain the plasma properties and show how the magnetic structure can support a prominence. Here we describe the 3D MHD model.

2.1. The MHD Model

To model magnetic structures in active regions we solve the following MHD equations in Cartesian geometry:

$$\nabla \times \mathbf{B} = \frac{4\pi}{c} \mathbf{J}, \quad (1)$$

$$\nabla \times \mathbf{E} = -\frac{1}{c} \frac{\partial \mathbf{B}}{\partial t}, \quad (2)$$

$$\mathbf{E} + \frac{\mathbf{v} \times \mathbf{B}}{c} = \eta \mathbf{J}, \quad (3)$$

$$\rho \left(\frac{\partial \mathbf{v}}{\partial t} + \mathbf{v} \cdot \nabla \mathbf{v} \right) = \frac{1}{c} \mathbf{J} \times \mathbf{B} + \nabla \cdot (\nu \rho \nabla \mathbf{v}). \quad (4)$$

\mathbf{E} and \mathbf{B} are respectively the electric and magnetic fields, \mathbf{v} is the plasma velocity, c the speed of light, η the resistivity, ν the viscosity, ρ is the plasma density assumed to be constant. The exclusion of the pressure gradient and gravity from the momentum equation is justified because the dynamics of an active region is dominated by the strong magnetic field, i.e. the corona is a low- β medium (where β is the ratio of the plasma and magnetic pressures). We use a $51 \times 51 \times 61$ nonuniform grid to mesh a cubic domain, $-2L < x < 2L$, $-2L < y < 2L$, $0 < z < 4L$, with $L = 1.5 \times 10^5$ Km. The Lundquist number S is defined as the ratio of the resistive diffusion time τ_R to the Alfvén time τ_A . In our model we have $S = 1 \times 10^5$, which is much lower than the value in the solar corona. This is necessary to dissipate structures that cannot be resolved since they are smaller than the cell size. However it does not influence the large scale dynamics in which we are interested. For the same reason we choose ν such that the ratio of the viscous dissipative time vs. the Alfvén time is $\tau_\nu/\tau_A = 200$.

2.2. The Simulation

The MHD simulation can be divided into three main phases. In the first phase of our simulation we specify a magnetic flux distribution at the base of our domain. It consists of the superposition of three Gaussian distributions and captures the salient features of the bipolar region surrounding the prominence of September 23, 1996 (Fig. 1). We do not attempt to model this region in detail. We are merely seeking to model the large-scale magnetic topology as simply as possible. Then we find the corresponding potential magnetic field for this flux distribution, some representative field lines of which are shown in Fig. 2a.

In the second phase we apply a velocity shear on the lower boundary surface for a specified duration, localized along the neutral line and advance Eqs. (3-4) in time. The form of the shear is

$$\mathbf{v}_b = \nabla \times \psi(x, y) \hat{\mathbf{z}}, \quad (5)$$

where ψ is a specified scalar function. If we choose $\psi = \psi(B_z)$, it can be shown that the flow derived from Eq. (5) preserves the original magnetic flux of the configuration (Amari et al. 1996). The corresponding flow consists of two vortices rotating in the same direction and centered on the opposite polarity regions. The maximum speed of the flow is set to one hundredth of the Alfvén speed. The system evolves through a series of force-free, increasingly sheared equilibria. With this flow pattern we do not intend to model a physical process by which the prominence is actually formed but we only use it as a method to form such equilibria with a given surface flux distribution. Figure 2b shows some field lines at the end of the shearing phase.

Finally, in the third phase we reduce the magnetic flux at the photospheric boundary as in Amari et al. (1999). The magnitude of the original magnetic flux decreases by 20%. Our experience tells us that the exact change in the flux distribution is not important as long as the total flux is reduced. It is during this last phase that magnetic reconnection

occurs and a flux rope is formed (Fig. 2c). The flux rope, which is surrounded by an almost potential arcade, lies along the neutral line. The magnetic field in the flux rope has dips; we will show how the cold and dense material typical of a prominence can be stored in there.

3. Dips and Condensations

Our philosophy is to separate the calculation in two parts. In the previous section we have obtained the magnetic field with the 3D MHD model. In order to see if the magnetic field can support a condensation, we now proceed to find the plasma properties, ρ and T , along selected field lines with a 1D hydrodynamic model. This can be done because the plasma is low β and the perturbation to \mathbf{B} due to pressure gradients and gravity is small. We solve the following equations:

$$\frac{\partial \rho}{\partial t} + v \frac{\partial \rho}{\partial s} = -\rho \frac{1}{A} \frac{\partial}{\partial s} A v, \quad (6)$$

$$\frac{\partial T}{\partial t} + v \frac{\partial T}{\partial s} = -(\gamma - 1) T \frac{1}{A} \frac{\partial}{\partial s} A v - (\gamma - 1) \frac{m_p}{k \rho} \left(\frac{1}{A} \frac{\partial}{\partial s} A \kappa_0 T^{5/2} \frac{\partial T}{\partial s} + n_e n_p Q(T) - H \right) \quad (7)$$

$$\frac{\partial v}{\partial t} + v \frac{\partial v}{\partial s} = -\frac{1}{\rho} \frac{\partial p}{\partial s} - g_s + \frac{1}{\rho A} \frac{\partial}{\partial s} A \left(\nu \rho \frac{\partial v}{\partial s} \right). \quad (8)$$

s is the length element along the field line; T , p and ρ are the plasma temperature, pressure and density; k is Boltzmann constant; $A(s) = B_0/B(s)$ is the expansion factor of the field line; κ_0 is Spitzer coefficient for thermal conduction ($\kappa_{\parallel} = \kappa_0 T^{5/2}$); $\gamma = 5/3$ is the ratio of specific heats; Q is the radiation law [see Athay (1986)]; n_e and n_p are the electron and proton number density and are equal in our calculation; $H = H_0 \exp(-(r - R_{\odot})/\lambda)$ is a parameterized heating function; $g_s = \mathbf{g} \cdot \hat{\mathbf{b}}$ is the projected gravitational force; m_p is the proton mass and $\rho = m_p n_p$.

According to Rosner et al. (1978), in the case of low-lying (constant pressure) loops there exists a lower limit L_H for the length scale λ of an exponentially decaying heating function in order to have a solution with maximum temperature in the middle. This limit

is proportional to the length of the loop L . The presence of gravity does not fundamentally change this result (Serio et al. 1981). When $\lambda < L_H$ only a solution with a temperature minimum in the middle is possible. The presence of a condensation in the middle can be thought as splitting the loop in two of length $L/2$. This effectively decreases L_H to $L_H/2$ and if $\lambda > L_H/2$ then the solution with condensation in the middle is stable. Our choice for all simulations is $\lambda = 0.05 R_\odot$. H_0 is chosen to give a surface energy flux of $10^6 \text{ erg cm}^{-2} \text{ s}^{-1}$.

As an initial state we choose an arbitrary temperature profile and calculate the corresponding pressure and density from solving Eq. (8) with $v = 0$. The temperature profile is chosen such that the system is not in thermal equilibrium. Equations (6-8) are advanced to steady state using rigid wall boundary conditions at the ends of the loops (we have tested the stability of the final states by continuing the simulations with free-flow conditions (Antiochos et al. 1985; Mok et al. 1991). With these boundary conditions at $s = 0$ and $s = L$ a dense and cold chromosphere is formed, next to a transition region with sharp gradients. In the interior we have a hot, tenuous corona. Two kind of solutions are possible: with and without condensation. Loops with a height profile as in Fig. 3 (i.e., loops in the overlying arcade) do not support a condensation. In fact an eventual condensation forming at the top of the loop would be unstable to the Rayleigh-Taylor instability (dense material on top of tenuous). The solution is the classical loop solution with temperature maximum and density minimum at the top. These loops constitute the arcade surrounding the flux rope. However, when a dip is present in the magnetic field line as in Fig. 4, then the configuration is able to sustain the condensation. This occurs for the field lines that belong to the flux rope.

A composite plot of all the simulations performed is presented in Fig. 5. The temperature and logarithmic density along the field lines is indicated in a color scale.

Condensations appear to be associated with the dips of the flux ropes and are absent in the semi-circular loops. The images can be compared with Fig. 1, and they show how it is the superposition of several single condensations that forms the prominence.

4. Conclusions

We have shown how the process of canceling and dispersal of magnetic flux in a sheared realistic magnetic configuration can lead to the formation of a flux rope. Our simulation is intended to model the prominence that was visible on September 23, 1996. Solutions of the hydrodynamic equations with thermal conduction, heating and radiation losses were performed along the field lines of the final state. They show that the dips in the magnetic field lines in the flux rope can support the dense and cold material typical of a prominence. Arcade-like field lines do not have dips and are therefore incapable of confining the heavy material against gravity. The superposed view of all the condensations appears as a prominence.

Real filaments have barbs also, which are curved feet connecting the body of the filament to the chromosphere. We plan to use our model with a more realistic magnetic flux distribution that includes parasitic polarities, which may be able to reproduce barbs. We have not addressed the point of how the prominence is actually formed, either via evaporation and successive condensation of chromospheric material or through mechanical lifting of cold and dense matter during the reconnection phase. In order to investigate this issue a more sophisticated model is needed, which should include a self-consistent 3D MHD simulation with an energy equation incorporating coronal heating, thermal conduction and radiation losses. This will be studied in the future.

Acknowledgments. The authors gratefully acknowledge the support of the National

Aeronautics and Space Administration (Sun-Earth Connections Theory Program, Supporting Research and Technology Programs, and SOHO Guest Investigator Program) and the National Science Foundation (Space Weather Program ATM9613834) in undertaking this study. We also thank the National Science Foundation at the San Diego Supercomputer Center and the National Energy Research Supercomputer Center for providing computational support.

REFERENCES

- Amari, T., Luciani, J. F., Aly, J. J., Tagger, M. 1996, ApJ, 466, L39
- Amari, T., Luciani, J. F., Mikić, Z., and Linker, J. 1999, ApJ, 518, L57
- Antiochos, S. K., Shoub, E. C., An, C. H., and Emslie, A. G. 1985, ApJ, 298, 876
- Antiochos, S. K., Dahlburg, R. B., and Klimchuk, J. A. 1994, ApJ, 420, L41
- Antiochos, S. K., MacNeice, P. J., Spicer, and Klimchuk, J. A. 1999, ApJ, 512, 985
- Athay, R. G. 1986, ApJ, 308, 975
- Dahlburg, R. B., Antiochos, S. K., and Klimchuk, J. A. 1998, ApJ, 495, 485
- Mok, Y., Schnack, D. D., and Van Hoven, G. 1991, Sol. Phys., 132, 95
- Priest, E. R. 1982, Solar Magnetohydrodynamics (Dordrecht: Reidel)
- Rosner, R., Tucker, W. H., and Vaiana, G. S. 1978, ApJ, 220, 643
- Serio, S., Peres, G., Vaiana, G. S., Golub, L., and Rosner, R. 1981, ApJ, 243, 288
- Zirker, J. B., Engvold, O., and Martin, S. F. 1998, Nature, 396, 440.

Fig. 1.— $H\alpha$ image of the prominence of September 23, 1996 from the National Solar Observatory/Sacramento Peak, Sunspot NM (left). Corresponding magnetogram from the Kitt Peak National Observatory AURA/National Solar Observatory/National Science Foundation (right).

Fig. 2.— Magnetic field lines during the three phases of the simulation: (a) potential field; (b) localized shearing along the neutral line; (c) emergence of opposite polarity flux and flux rope formation, surrounded by an arcade. Underlying is the magnetic flux distribution.

Fig. 3.— Height (top), temperature (middle) and density (bottom) profile as a function of the distance along the field line for a configuration that does not develop a condensation. No dip is present to sustain a stable condensation.

Fig. 4.— Height (top), temperature (middle) and density (bottom) profile a function of the distance along the field line for a configuration that develops a condensation. The condensation appears in the dip of the field line.

Fig. 5.— Temperature (top row) and density (bottom row) along several field lines and three different views from left to right. Arcade-like loops do not develop a condensation. Field lines forming the flux rope show that condensations occur in the dips. The combined view forms the prominence.

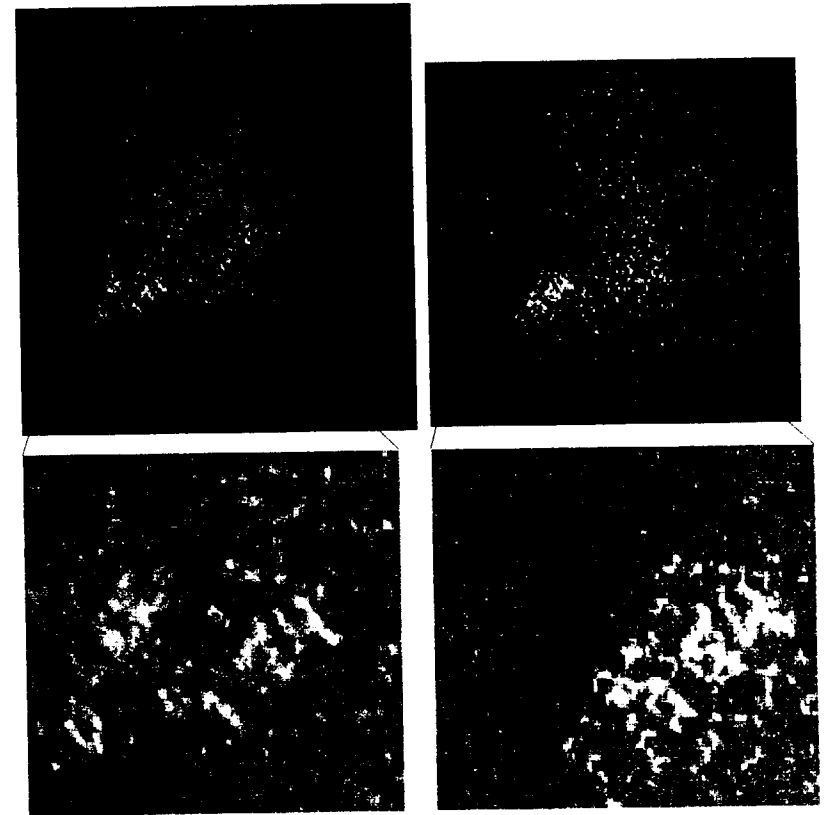


Fig. 1.—



Fig. 2.—

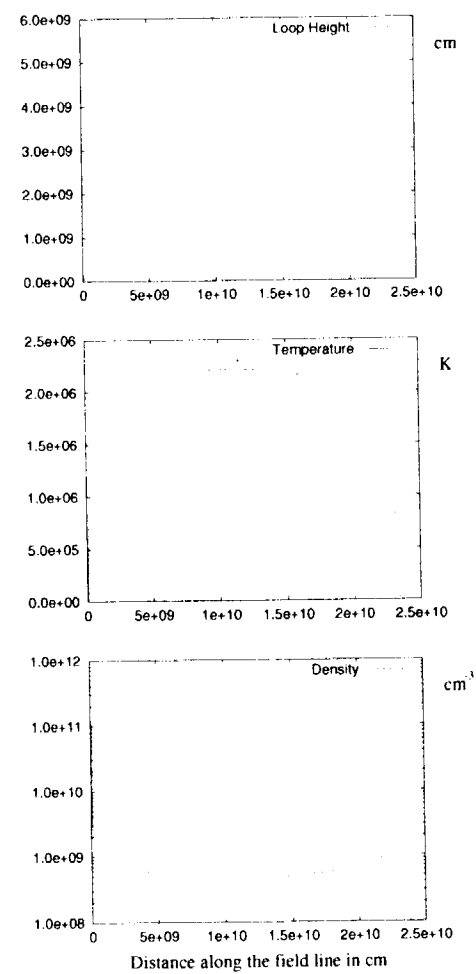


Fig. 3.—

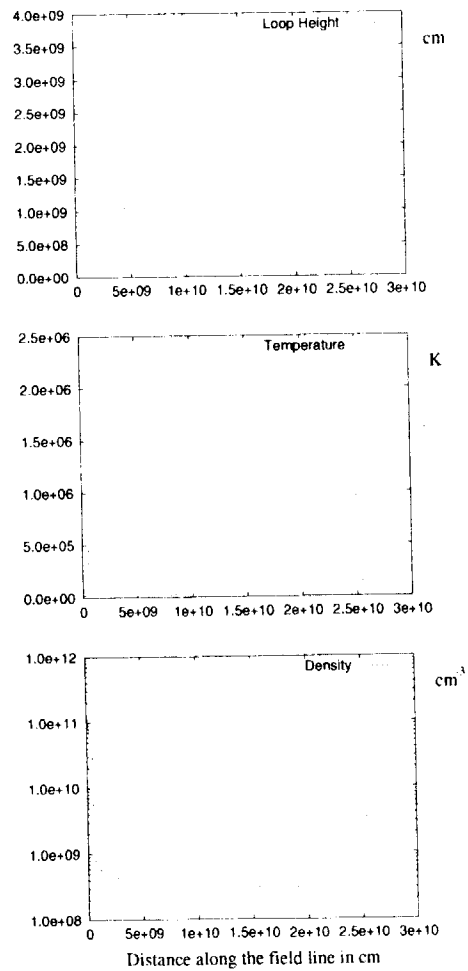


Fig. 4.—

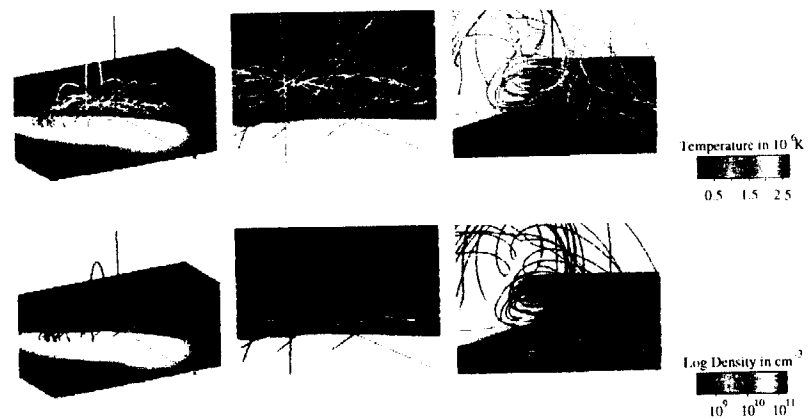


Fig. 5.—

APPENDIX B

“An Empirically-Driven Global MHD Model of the Solar Corona and Inner Heliosphere”

P. Riley, J. A. Linker, and Z. Mikić

Accepted for publication in *Journal of Geophysical Research*

An Empirically-Driven Global MHD Model of the Solar Corona and Inner Heliosphere

Pete Riley, J. A. Linker, and Z. Mikić
Science Applications International Corporation, San Diego, California

Short title: MHD MODEL OF THE HELIOSPHERE

Abstract.

In this study we describe a three-dimensional MHD model of the solar corona and heliosphere. We split the modeling region into two distinct parts: the solar corona (1 solar radius, R_s , to $30 R_s$) and the inner heliosphere ($30 R_s$ to 5 AU). This combined model is driven solely by the observed line-of-sight photospheric magnetic field and can thus provide a realistic global picture of the corona and heliosphere for specific time periods of interest. We use the model to illustrate heliospheric structure during three different phases of the solar cycle: (1) Carrington Rotation (CR) 1913 (August 22, 1996 – September 18, 1996), which occurred near solar minimum and overlapped the “Whole Sun Month” campaign; (2) CR 1892 (January 27, 1995 – February 23, 1995), which occurred during the declining phase of cycle 22 and coincided with the so-called “Ulysses rapid latitude scan”; and (3) CR 1947 (March 7, 1999 – April 4, 1999), which occurred approximately 15 months before the predicted maximum of solar cycle 23. We compare Ulysses and WIND observations with the simulation for CR 1913 and compare Ulysses observations during its traversal from pole to pole with CR 1892. We find that the simulations reproduce the overall large-scale features of the observations. We use the near solar maximum results to speculate on the structure of the high-latitude solar wind that Ulysses will encounter during its traversal of the southern and northern solar poles in 2000 and 2001, respectively. In particular, the results suggest that, due to the presence of equatorial coronal holes, the ordered pattern of CIR tilts and their associated shocks, that was observed during Ulysses initial southward excursion in 1992, will likely disappear completely as Ulysses moves toward the south pole. We anticipate that Ulysses will encounter fast streams but will not remain within them for more than a fraction of a solar rotation. Finally, the simulations suggest that crossings of the HCS will persist up to at least $\sim 70^\circ$ heliographic latitude.

1. Introduction

Beyond ~ 10 solar radii (R_s), solar material streams away from the Sun along roughly radial trajectories. A combination of temporal variations at the Sun, together with the rotation of the Sun, leads to parcels of plasma with different plasma and magnetic properties becoming radially aligned: faster material overtaking slower material leads to a compression front, while slower material being outrun by faster material leads to a rarefaction region, or expansion wave [Sarabhai, 1963]. When the flow pattern at the Sun does not vary considerably during a solar rotation (such as during solar minimum), the large-scale compressive structures created by the interaction of these streams are fixed in a frame corotating with the Sun, and they are known as Corotating Interaction Regions (CIRs) [Smith and Wolfe, 1976]. When the difference in speed between the slow and fast streams is sufficiently large, a pair of shocks may form bounding the CIR [e.g., Pizzo, 1985].

During its initial voyage out of the ecliptic plane, Ulysses observed a systematic tilt to CIRs [Gosling *et al.*, 1993, 1995a; Riley *et al.*, 1996]. These interaction regions were observed from January, 1992 to October, 1999, corresponding to the declining phase of solar cycle 22. In the azimuthal (ϕ) plane, their outward normals were tilted westward (i.e., into the direction of planetary motion). This was to be expected, as the interaction regions aligned themselves roughly along the direction of the Parker spiral. In the meridional plane (θ), their outward normals were tilted toward the heliographic equator. These results were supported by numerical MHD simulations [Pizzo and Gosling, 1994] which suggested that these orientations were a natural consequence of the tilt of the solar magnetic-dipole axis relative to the solar rotation axis. This pattern of tilts was once again observed during Ulysses' so-called "rapid latitude scan" [Gosling *et al.*, 1995b] and most recently, as Ulysses descended from the northern polar regions to the equator (during solar minimum and the early/mid ascending phase of cycle 23) [Gosling *et al.*, 1997; McComas *et al.*, 1998a].

Previous solar wind models have yielded considerable insight into the dynamical processes that shape the structure of the heliosphere. The large-scale, time-stationary structure of the heliosphere under an idealized tilted-dipole geometry was studied by Pizzo [1991, 1994a]. At an inner boundary of $32 R_s$, a flow pattern was constructed consisting of slow, dense flow about a heliomagnetic equator that was tilted by a specified amount relative to the rotational axis. Similar simulations were used by Gosling and Pizzo [1994] to interpret Ulysses observations at mid-heliographic latitudes, where it was found that CIR-associated reverse shocks persist to much higher latitudes than CIR-associated forward shocks. In both cases, the tilted dipole geometry at the inner boundary strongly drives the position and orientation of the CIRs and their associated shocks. In particular, under moderately low solar activity conditions, CIRs and shock outward normals are tilted toward the equator in both hemispheres. Thus, in the ecliptic plane, a spacecraft samples alternating tilts as it passes through a predominantly northern hemispheric CIR, and subsequently a predominantly southern-hemispheric CIR. Moreover, the strongest interactions take place away from the ecliptic plane, at latitudes roughly equal to the tilt of the solar dipole relative to the rotation axis.

Wang and Sheeley [1990] exploited an empirical relationship between solar wind speed and coronal flux-tube expansion [Levine *et al.*, 1977] to predict solar wind speed at 1 AU and beyond. They found that coronal flux tubes that expand more slowly correlate with faster asymptotic speed along that flux tube. Using this relationship, they predicted the types of wind speed patterns that Ulysses would be expected to see during its second solar orbit [Wang and Sheeley, 1997]. In particular, they predicted that the ascending phase of the solar cycle would be dominated by recurrent (28–29 day periodicity), high-speed streams originating from high-latitude extensions of polar coronal holes. Approaching solar maximum, however, persistent high-speed streams would disappear, only to be replaced by low-speed wind at all latitudes. Finally, at solar maximum (or more specifically at the time that the polar field reverses), very fast

episodic polar jets would be generated as active region fields migrated toward the solar poles.

Usmanov et al. [2000] developed an axisymmetric MHD model of the corona and inner heliosphere. Their technique relies on outwardly propagating Alfvén waves to provide all of the heating and acceleration of the solar wind flow. In reality, it is likely that a complex combination of thermodynamic processes is necessary to accurately describe the heating and acceleration of the solar wind [*Lionello et al.*, 2000]. Nevertheless, their approach quantitatively reproduces Ulysses’ plasma and magnetic field observations during the rapid latitude scan. Since the model is two-dimensional, no interaction regions are produced. In spite of this, their success suggests that such an approach in three dimensions might represent an effective compromise between a complex treatment that includes a transition region and coronal heating mechanisms [e.g., *Lionello et al.*, 2000] and a more limited polytropic approach [e.g., *Riley et al.*, 2000].

The heliospheric current sheet (HCS) is a global structure in the heliosphere that separates inwardly- and outwardly-directed magnetic field lines. It plays an important role in the modulation of cosmic rays and energetic particles in the solar wind. Simple models of the HCS have been constructed that ballistically trace out the inferred locus of the neutral line at the Sun [e.g., *Jokipii and Thomas*, 1981]. However, by not accounting for the deformation of the HCS through the evolution of interaction regions, these models can at best provide only a qualitative picture of the shape of the HCS. In contrast, *Pizzo* [1994b] used an idealized 3-D, steady-state MHD model to simulate the structure of the HCS out to 30 AU for the tilted-dipole geometries discussed above. He found that for dipole tilts larger than $\sim 10^\circ$, noticeable deformation of the HCS occurred within 5 AU, and by ~ 10 AU (where CIR-associated shocks had overtaken the HCS) significant distortion of the HCS occurred. *Pizzo* emphasized the importance of the HCS as a global structure about which the interaction regions are organized.

The data utilized in this study derives from the Solar Wind Over the Poles of the Sun (SWOOPS) ion sensor [*Bame et al.*, 1992] and the magnetic field investigation [*Balogh et al.*, 1992] on board the Ulysses spacecraft and from the Faraday cup instrument on board WIND [*Ogilvie et al.*, 1995]. The plasma moments produced from the Ulysses measurements have a typical resolution of 4-8 mins while moments produced from WIND measurements have a resolution of 90 secs. All data presented here, however, have been averaged over at least 1 hour.

The purpose of this report is two-fold. First to introduce an empirically-driven, time-dependent, 3D resistive MHD model of the corona and heliosphere. To test its applicability, we make comparisons with WIND and Ulysses observations during a relatively quiet period of the solar cycle. We use the model to explore how the large-scale structure of the heliosphere changes over the course of a solar cycle. We then use these results to make basic predictions about the large-scale structure Ulysses may find at high heliographic latitudes during its second orbit at solar maximum. This report is structured as follows. In section 2 we introduce the basic features and limitations of the model. In sections 3, 4, and 5, we model the structure of the heliosphere at three time periods corresponding to solar minimum, the declining phase, and solar maximum conditions, respectively. In section 6 we explore the variability of the HCS for the aforementioned time periods. Finally, in section 7 we summarize the results of this study and speculate on what Ulysses may see when it traverses the poles of the Sun at solar maximum.

2. Description of the Model

2.1. Equations and Solution Technique

In recent years, we have developed a 3-D, time-dependent resistive MHD model to investigate the structure of the solar corona [e.g., *Mikić et al.*, 1999; *Linker et al.*, 1999].

We solve the following system of partial differential equations, in spherical coordinates:

$$\nabla \times \mathbf{B} = \frac{4\pi}{c} \mathbf{J} \quad (1)$$

$$\frac{1}{c} \frac{\partial \mathbf{B}}{\partial t} = -\nabla \times \mathbf{E} \quad (2)$$

$$\mathbf{E} + \frac{\mathbf{v} \times \mathbf{B}}{c} = \eta \mathbf{J} \quad (3)$$

$$\frac{\partial \rho}{\partial t} + \nabla \cdot (\rho \mathbf{v}) = 0 \quad (4)$$

$$\rho \left(\frac{\partial \mathbf{v}}{\partial t} + \mathbf{v} \cdot \nabla \mathbf{v} \right) = \frac{1}{c} \mathbf{J} \times \mathbf{B} - \nabla p + \rho \mathbf{g} + \nabla \cdot (\nu \rho \nabla \mathbf{v}) \quad (5)$$

$$\frac{\partial p}{\partial t} + \nabla \cdot (p \mathbf{v}) = (\gamma - 1) (-p \nabla \cdot \mathbf{v} + S) \quad (6)$$

where \mathbf{B} is the magnetic field intensity; \mathbf{J} is the electric current density; \mathbf{E} is the electric field; \mathbf{v} is the plasma velocity; ρ is the plasma mass density; p is the gas pressure; \mathbf{g} is the acceleration due to gravity; γ is the ratio of specific heats; η is the plasma resistivity; ν is the kinematic viscosity, and S represents energy source terms.

In this study, we approximate the energy equation with a simple adiabatic energy equation (i.e., $S = 0$) and choose the polytropic index (γ) to be 1.05 in the coronal model and 1.5 in the heliospheric model. The coronal value reflects the fact that temperature does not vary significantly in the corona. While this approximation significantly simplifies the calculation and reduces the time necessary to complete a simulation, the resultant plasma parameters predicted by the model do not show the same degree of variation as is inferred from in situ and solar observations. In the heliosphere, on the other hand, a polytropic relationship between pressure and density is observed to hold, with $\gamma \sim 1.5$ for protons (e.g., *Totten et al.* [1995]; *Feldman et al.* [1998]).

The details of the algorithm used to advance the MHD equations are provided elsewhere [*Mikić and Linker*, 1994; and *Lionello et al.*, 1998]. Here we briefly make a

few remarks. In the radial (r) and meridional (θ) directions we use a finite-difference approach. In azimuth (ϕ), the derivatives are calculated pseudo-spectrally. We impose staggered meshes in r and θ that have the effect of preserving $\nabla \cdot \mathbf{B} = 0$ to within round-off errors for the duration of the simulation. The simulations discussed here were performed on (r, θ, ϕ) grids ranging from $81 \times 81 \times 64$ to $121 \times 121 \times 128$.

It is convenient to separate the region between the solar photosphere and the Earth into two parts. We distinguish between the more complex “coronal” region, which includes the region from the photosphere up to $20\text{--}30 R_\odot$, and the “heliospheric” region, which covers the region of space between $30 R_\odot$ and 1.5 AU. In the latter, the flow is everywhere supersonic, gravity can be neglected (although it is included for completeness), and the energy equation can be reasonably approximated by a polytropic relationship. Thus the time step required to advance the solution in the heliospheric model is considerably larger than the time step required for the coronal solution. Computationally then, it is more efficient to advance the heliospheric portion of the simulation independently of the coronal time step.

Ultimately, our goal is to use the output of the coronal solution directly to provide the inner boundary condition of the heliospheric model. At present, however, the plasma speed predicted by the polytropic coronal model is not sufficiently high to drive the heliospheric model. The recent addition of a more complex thermodynamic treatment of the energy equation [*Lionello et al.*, 2000] promises to yield more realistic plasma parameters; however, this refinement is still under development and requires further validation. Thus both as an interim solution, and as a practical and computationally-inexpensive approach, we have developed a technique for deducing speed, density, and temperature, based on the magnetic topology of the coronal solution (which is probably the most accurately determined property of the coronal model).

2.2. Modeling the Solar Corona

Coronal calculations are typically performed between $1 R_s$ (i.e., the base of the corona) and $20\text{--}30 R_s$, although we have positioned the outer boundary as far away as $1\text{--}2 \text{ AU}$ [e.g., *Linker and Mikić, 1997*]. At the lower boundary, we specify the radial component of the magnetic field, B_r , based on the observed line-of-sight measurements of the photospheric magnetic field, and uniform, characteristic values for the plasma density and temperature. An initial estimate of the field and plasma parameters are found from a potential field model and a Parker transonic solar wind solution [*Parker, 1963*], respectively. This initial solution is advanced in time until a steady state is achieved.

2.3. Modeling the Heliosphere

The heliospheric calculation is initiated using the results of the coronal solution. To determine the inner heliospheric boundary conditions (at $r = 30 R_s$), we use the magnetic field topology of the coronal solution. We assume that within coronal holes (i.e., away from the boundary between open and closed magnetic field lines) the flow is fast. At the boundary between open and closed field lines, the flow is slow. Over a relatively short distance, we smoothly raise the flow speed to match the fast coronal hole flow. We specify the photospheric flow field as follows.

$$v_r(d) = v_{slow} + \frac{1}{2} (v_{fast} - v_{slow}) \left(1 + \tanh \left(\frac{d - \alpha}{w} \right) \right) \quad (7)$$

where d is the minimum distance from an open/closed boundary, measured along the surface of the photosphere, α is a measure of how thick the slow flow band is (~ 0.1 radians, or $\sim 6^\circ$), and w is the width over which the flow is raised to coronal hole values (~ 0.05 radians, or $\sim 3^\circ$). Although this approach is somewhat ad hoc, it is based on the commonly held view that slow flow originates from the boundary between open and closed field lines and fast flow originates in coronal holes. Once this speed map is

determined in the photosphere, it is mapped outward along field lines to generate the inner boundary of the heliospheric model at $30 R_s$. We emphasize that this approach is only a convenient method of generating the inner boundary conditions for the heliospheric solution. In reality, there is significant acceleration of the plasma between the photosphere and upper corona.

In addition to the approximations discussed above, we make the following assumptions. First, we neglect the effect of pickup ions, which are thought to dominate the internal energy of the solar wind beyond $6\text{--}10 \text{ AU}$ [*Axford, 1972*]. Thus we limit our modeling region to $< 5 \text{ AU}$. Second, we neglect the effects of differential rotation, which may play a role in connecting high latitude field lines near the Sun with lower-latitude interaction regions much further away [*Fisk, 1996*]. We assume that the inner boundary rotates rigidly with a period of 25.38 days. Third, although the MHD model is time-dependent, we assume that the flow at the inner boundary is time-stationary. Thus the flow is “corotating”, so that rotating spatial variations are responsible for the generation of dynamic phenomena in the solution.

We illustrate this technique in Figure 1 for the time period August 10 to September 8, 1996. This interval coincided with the campaign known as “Whole Sun Month.” (WSM) occurring just four months after the termination (minimum) of solar cycle 22, and has been the focus of considerable research (see papers in the special issue of *Journal of Geophysical Research*, May, 1999). In panel (a) we have traced coronal field lines to deduce whether they are open or closed. Regions in which the field lines are closed are shaded gray, and open field line regions are shaded black. In panel (b), we have shaded the photosphere according to the algorithm described above. Note that the central band, indicated with zero speed, does not contribute to the inner boundary conditions of the heliospheric model since the field lines there are all closed. In panel (c) we show the speed profile mapped along field lines to $30 R_s$. The mapping process has yielded a relatively complex flow pattern. In particular, the slow-speed band encircling

the equator contains significant spatial structure.

Using this recipe, we derive the flow speed at $30 R_s$. By imposing momentum flux balance at the inner radial boundary, we derive the plasma density. Theoretically, there is little justification for this assumption; however, Ulysses observations suggest that momentum flux is roughly conserved [Riley *et al.*, 1997]. To derive the temperature we impose thermal pressure balance. This is again, an ad hoc assumption, however, any significant pressure gradients would be quickly minimized by the flow. To complete the necessary inputs, we use the radial component of the magnetic field, B_r , directly from the coronal solution.

3. Structure of the Heliosphere at Solar Minimum

To illustrate the structure of the heliosphere during solar minimum conditions, we have modeled the WSM I time period (August 10 to September 8, 1996). Figure 2 summarizes the large-scale features of the heliosphere using the input flow speed shown in Figure 1c. The heliospheric current sheet (inferred from the iso-surface $B_r = 0$) is displayed out to 5 AU. A meridional slice of the radial velocity is shown at an arbitrary longitude. Blue corresponds to slowest speeds ($\sim 350 \text{ km s}^{-1}$) and red corresponds to fastest speeds ($\sim 750 \text{ km s}^{-1}$). Superimposed is a selection of interplanetary magnetic field lines, as well as the trajectories of the WIND and Ulysses spacecraft in a corotating frame. The structure portrayed in Figure 2 fits well with the general picture deduced from solar and interplanetary observations during this time period [e.g., Riley *et al.*, 1999; Linker *et al.*, 1999]. In particular, the streamer belt showed little ($< 10^\circ$) inclination relative to the heliographic equator, but was deformed northward at longitudes of $\sim 250 - 300^\circ$ (at the Sun) due to the presence of an active region. Note that in spite of the low inclination of the current sheet, by 4 AU it has developed considerable structure, including a fold back on itself.

Figure 3 summarizes the plasma and field parameters as viewed in a meridional

plane. The left panel shows color contours of radial velocity, the middle panel shows contours of number density (scaled by r^2 , to remove the fall off associated with the spherical expansion of a constant speed solar wind), and the right panel shows contours of gas, or thermal pressure (scaled by r^3 to remove the $1/r$ fall off associated with the near adiabatic ($\gamma = 1.5$) expansion of the wind, as well as the $1/r^2$ fall-off associated with the spherical expansion). In each panel, the location of the HCS is marked by the solid line.

Figure 4 provides a complementary view of the same simulation, showing the radial velocity, meridional velocity, azimuthal velocity, scaled number density, thermal pressure, and magnetic field magnitude, at a heliocentric distance of 2.3 AU. In each panel, the location of the HCS has been overlayed. The trajectory of a spacecraft located at a fixed point in space would trace a horizontal line from right to left in this display. Consider, for example, a hypothetical spacecraft located at 2.3 AU and 30° above the ecliptic plane. From the top-left panel, the spacecraft would sample predominantly fast solar wind for most of a rotation, with a relatively slow speed drop at $\sim 90^\circ$ and a relatively fast speed increase at $\sim 300^\circ$. By comparison with the bottom 3 panels, we would associate the speed increase with the presence of an interaction region (at $\sim 300^\circ$ longitude) and the speed decrease with the presence of an expansion wave (at $\sim 60^\circ$ longitude). From the top-middle panel, we deduce that the flow deflections through the interaction region are first positive and then negative in the meridional plane. In our coordinate system, a positive meridional velocity is equatorward. Thus the flow is deflected first equatorward and then poleward. These deflections are in the same sense as those observed by Ulysses out of the ecliptic plane and are consistent with the outward normal of the interaction region being tilted toward the heliographic equator [e.g., Pizzo and Gosling, 1994]. Similarly, we deduce from the positive, then negative flow deflections across the interaction region in the azimuthal plane (top-right panel) that the outward normal to the interaction region is tilted toward the west (i.e., into the

direction of planetary motion), or, alternatively, the interaction region is approximately aligned with the Parker spiral direction.

In Figure 5 we compare 1-hr averaged observations of speed, density, and temperature by the Ulysses spacecraft (squares) with simulation results (solid curves) during the WSM interval. At the time, Ulysses was returning to lower latitudes and was located at $\sim 28^\circ$ North heliographic latitude, at a distance of ~ 4.3 AU, and on the opposite side of the Sun from Earth. Thus the measurements of the line-of-sight photospheric magnetic field used to drive the solution were always separated by $\sim 180^\circ$ from the actual solar wind that Ulysses observed. The profile at Ulysses consisted of a simple, single stream pattern. The model appears to reproduce the essential features of the large-scale variations, i.e., the interaction region and the expansion wave; however, the interaction region is not as steep as the observations indicate, and the model does not reproduce fluctuations on scales less than a few days.

In Figure 6 we make an analogous comparison with WIND plasma data. WIND was located in the ecliptic plane at 1 AU and observed a more complex pattern of variations that are only partially reproduced by the MHD solution. The simulation predicts two fast ($> 500 \text{ km s}^{-1}$) streams, of which only one is obviously found in the observations (at day 255). The second (at day 240) may be related to the fast stream observed on day 243, although it is considerably broader. There are other minor perturbations in the model; however, none of them can be reliably matched with WIND observations.

4. Structure of the Heliosphere during the Declining Phase of the Solar Cycle

To illustrate the structure of the heliosphere during more active conditions, we have modeled Carrington rotation (CR) 1892 (day 27–55, 1995), which fell on the late declining phase of solar cycle 22. In Figure 7 we compare Ulysses plasma and magnetic

field observations during its so-called “rapid latitude scan” from September, 1994 (when it reached its most southern latitude of $S80^\circ$), to July, 1995 (when it reached its most northern latitude of $N80^\circ$) with simulation results. From top to bottom, the panels compare speed, scaled density, scaled temperature, and the radial component of the magnetic field, B_r . A two-day box-car running average has been applied to B_r to bring out large-scale variations. Although several rotations of the Sun occurred during this interval, the most-rapid traversal through the equator occurred during ~ 3 Carrington rotations (1892–4). During CR 1892, Ulysses moved from -27.6° to -6.9° and from 1.43 AU to 1.35 AU. The spacecraft crossed into the northern polar coronal hole on day 87, 1995 [McComas *et al.* 1998b], some 32 days after the end of CR 1892. Thus the comparison between simulation and observations is expected to be most appropriate during Ulysses’ initial immersion into the slow, dense solar wind. Unfortunately, this crossing of the polar coronal hole boundary was complicated by the passage of a coronal mass ejection that was embedded within the slow-fast boundary [Gosling *et al.* 1995c]. The CME structure is not included in the present simulations, which as noted earlier, assume that the flow and field pattern are time-stationary in a corotating frame of reference.

In spite of these shortcomings, the overall pattern of interaction regions in the simulation bears a strong resemblance to the observations. Although the majority of the interaction regions and expansion waves are reproduced in the simulations, their strengths do not match: densities are too high in the interaction regions, yet not low enough in the rarefactions; speed peaks are not high enough; and temperatures do not fall enough. Nevertheless, it is quite remarkable that the final interaction region and northern polar-hole crossing are well reproduced almost two rotations after CR 1892.

5. Structure of the Heliosphere Approaching Solar Maximum

As the Sun moves from solar minimum to solar maximum, the assumption that the flow pattern at the Sun remains constant for an entire solar rotation begins to break down. CMEs and other transient phenomena play an ever increasing role in the dynamical evolution of the heliosphere. Nevertheless, we can still speak of a “rotationally-averaged” picture of the heliosphere during solar maximum conditions. Thus we restrict our use of solar maximum simulations to describe generic features of the heliosphere, and use the models to predict what Ulysses may see when it traverses the southern and northern poles in 2000 and 2001, respectively.

Figure 8 shows how the assumed radial velocity profile in the photosphere maps into the input conditions for the heliospheric solution. The time period modeled (days 66-94 of 1999) corresponds to CR 1947. Figure 8a shows the velocity profile in the photosphere, where again, the large expanse of zero speed (purple) corresponds to closed magnetic field lines and thus does not contribute to the coronal input conditions. Figure 8b shows the input speed profile at $30R_s$. Comparison of Figure 8 with Figure 1b and 1c highlights some striking differences between solar wind flow near the Sun at the minimum and maximum of the activity cycle. Whereas at solar minimum the slow wind is confined to a relatively narrow band organized about the equator, at solar maximum slow solar wind dominates the flow at essentially all heliographic latitudes. This is in agreement with the conclusions reached by *Wang and Sheeley* [1997]. A second noteworthy point concerns the way features are mapped out from the photosphere to the upper corona. At solar minimum (Figure 1), there is a fairly straightforward mapping between the two regions, indicating that the topology of the field lines is relatively simple. In contrast, at solar maximum, the relationship appears to be more complex. For example, all of the the source of the fast solar wind emanating from the south pole at $30 R_s$ maps to a photospheric source that is limited in longitudinal extent. Based on the photospheric sources of these flows, it is clear that it would be difficult to predict the

morphology of the flows in the upper corona without a model such as the one described here.

Figure 9 presents meridional slices of radial velocity, scaled number density, and scaled thermal pressure for CR 1947. The location of the HCS is again superimposed (solid line). These images may be compared with those in Figure 3. Several differences are apparent. First, the symmetric picture characteristic of solar minimum is lost at solar maximum. In the northern hemisphere, for example, we see the interaction of an isolated high-speed stream with slower solar wind ahead of it: an interaction region develops at the interface, bounded by a forward (ahead) and reverse (behind) wave. At lower heliographic latitudes, we see the effects of the interaction of medium-speed flow with slower flow. In particular, at $\sim S30^\circ$ the two strongest mid-latitude streams (located at $\sim 0 - 60^\circ$ longitude in Figure 8) are driving an interaction region whose outward normal is essentially radial. Finally, the interface between slow and fast solar wind at the southern coronal hole drives an interaction region (just visible at 5 AU and $\sim S60^\circ$) whose outward normal is tilted toward the heliographic equator.

Figure 10 shows spherical slices of the three velocity components (top panels) and density, thermal pressure, and magnetic field magnitude (bottom panels) for CR 1947. These images may be compared with those in Figure 4. Note that the heliospheric current sheet extends up to $\sim 55^\circ$ latitude in the northern hemisphere and $\sim 40^\circ$ in the southern hemisphere. As we have noted earlier, the pattern near solar maximum is much more complex. At, and near, solar minimum, the interaction and rarefaction regions develop a pattern of opposing tilts in each hemisphere [e.g., *Pizzo and Gosling*, 1994], so that the fronts run from low latitudes in the east to high latitudes in the west in both hemispheres. In contrast, at solar maximum, any orientation of interaction regions are possible, as is particularly evident from the color contours of number density (bottom-left panel) and thermal pressure (bottom-middle panel). Note that the small-scale peaks in density and pressure in Figures 4 and 10 arise from the limited

spatial resolution in the calculation. A limited number of higher-resolution simulations were run to demonstrate that: (1) such features disappear when sufficient resolution is present; and (2) the results are not qualitatively affected by the limited resolution.

6. The HCS at Different Phases of the Solar Cycle

The HCS is a convenient feature to illustrate the variability of the heliosphere during the solar cycle: being passive, it acts as a tracer for the macroscopic structure of the heliosphere [e.g., *Riley et al.*, 1996]. In Figure 11, we use the simulation results described here to illustrate the evolution of the HCS during the course of a solar cycle. The first panel shows the HCS near solar minimum. The single fold in the surface maps back to $\sim 180 - 270^\circ$ longitude. From Figure 1, it can be seen to correspond to the northward extension of the slow flow band. Note that this fold is radially asymmetric, with its outer edge being sharper than its inner edge. Referring to Figure 1, fast solar wind at $\sim 280^\circ$ overtakes slower wind ahead accelerating it and steepening the HCS profile. Conversely, at the inner edge of the deformation ($\sim 180^\circ$ longitude in Figure 1), the HCS is “stretched out” as faster wind outruns slower wind creating a rarefaction region. It is likely that this picture will differ from the ones produced by kinematic models of the HCS, which assume that the speed of the plasma remains constant as the plasma moves out from the Sun [e.g., *Sanderson et al.*, 1999]. In the middle panel, the HCS during the time of Ulysses’ “rapid latitude scan” is shown. Now two folds dominate the HCS profile and are in qualitative agreement with the picture built up by *Smith et al.* [1995] based on in situ crossings of the HCS by Ulysses. Finally, we present the HCS for CR 1947 in the bottom panel. The HCS is again dominated by two folds that extends up to $\sim 40 - 55^\circ$. In contrast to solar minimum, however, the folds are more symmetric, since the wind surrounding it does not have the same large variations in speed.

7. Summary and Discussion

Global MHD models provide a useful contextual basis with which to interpret coronal and solar wind observations. In this study, we have introduced a 3-D resistive MHD model of the solar corona and heliosphere, driven by the observed line-of-sight photospheric magnetic field. We have illustrated its use by simulating three specific time periods corresponding to solar minimum, the declining phase of the solar cycle, and near-solar maximum conditions. We find that the model reproduces the essential features of the observations at solar minimum and during the declining phase.

The near-solar maximum simulations suggest lower, more variable speeds and the absence of fast streams over a much broader range of heliolatitudes, in agreement with IPS measurements and recent Ulysses observations (<http://swoops.lanl.gov/recentvu.html>). Our simulations suggest that the pattern of alternating tilts that dominated Ulysses observations during its first orbit will likely be lost at solar maximum. To produce this pattern of “alternating tilts”, slow solar wind must emanate from lower latitudes than fast wind. Near solar minimum, this is accomplished because a band of slow solar wind is organized about the solar equator. Either a simple tilted-dipole band [*Pizzo*, 1991] (where the wind is organized about the magnetic equator which is tilted with respect to the rotation axis), or a warped band (where a warped flow is organized about the rotation axis) is sufficient to produce a regular pattern of alternating tilts. On the other hand, when isolated coronal holes (i.e., regions of faster wind completely encircled by slower wind) are present, the simple tilted fronts are replaced by more complex shapes. In the simplest case, a spherical coronal hole at low- or mid-latitudes would produce a U-shaped interaction region in the solar wind. Depending on a spacecraft’s latitude relative to the center of the disturbance, it would see a variety of orientations.

Based on the results presented here (and others not shown), we can make some predictions as to the nature of the solar wind that Ulysses will encounter during its crossings of the polar regions. First, the simulations suggest that while Ulysses may

encounter fast (i.e., $\sim 750 \text{ km s}^{-1}$) streams, it will likely not remain in them for more than a fraction of a solar rotation. This is in agreement with the predictions made by Wang and Sheeley [1997]. As discussed above, although the pattern of "alternating tilts" at Ulysses will likely disappear at low- and mid-heliographic latitudes, if a polar coronal hole is present, this pattern may return. Finally, the results suggest that crossings of the HCS may persist up to $\sim 70^\circ$ heliographic latitude.

Acknowledgments. The authors gratefully acknowledge the support of the National Aeronautics and Space Administration (Sun-Earth Connections Theory Program, Supporting Research and Technology Programs, and SOHO Guest Investigator Program) and the National Science Foundation (Space Weather Program ATM9613834) in undertaking this study. We also thank National Science Foundation at the San Diego Supercomputer Center and the National Energy Research Supercomputer Center for providing computational support.

References

- Axford, W. I., Interaction of the solar wind with the interstellar medium, in Solar Wind, edited by C. P. Sonett, P. J. Coleman, and J. M. Wilcox, *NASA Spec. Publ., NASA SP-308*, 609, 1972.
- Bane, S. J., D. J. McComas, B. L. Barraclough, J. L. Phillips, K. J. Sofaly, J. C. Chavez, B. E. Goldstein, and R. K. Sakurai, The Ulysses solar wind plasma experiment, *Astron. and Astrophys., Suppl. Ser.*, **92**, 237, 1992.
- Balogh, A., T. J. Beek, R. J. Forsyth, P. C. Hedgecock, R. J. Marquedant, E. J. Smith, D. J. Southward, and B. T. Tsurutani, The magnetic field investigation on the Ulysses mission: Instrumentation and preliminary scientific results, *Astron. Astrophys.*, **92**, 221, 1992.
- Feldman, W. C., B. L. Barraclough, J. T. Gosling, D. J. McComas, P. Riley, B. E. Goldstein, and A. Balogh, Ion energy equation for the high-speed solar wind: Ulysses observations, *J. Geophys. Res.*, **103**, 14,547, 1998.
- Fisk, L. A., Motion of the footpoints of heliospheric magnetic field lines at the Sun: Implications for recurrent energetic particle events at high heliographic latitudes, *J. Geophys. Res.*, **101**, 15,547, 1996.
- Gosling, J. T., S. J. Bane, D. J. McComas, J. L. Phillips, V. J. Pizzo, B. E. Goldstein, and M. Neugebauer, Latitudinal variation of solar wind corotating stream interaction regions: Ulysses, *Geophys. Res. Lett.*, **20**, 2789, 1993.
- Gosling, J. T., S. J. Bane, D. J. McComas, J. L. Phillips, V. J. Pizzo, B. E. Goldstein, and M. Neugebauer, Solar wind corotating stream interaction regions out of the ecliptic plane: Ulysses, *Space Sci. Rev.*, **72**, 99, 1995a.
- Gosling, J. T., W. C. Feldman, D. J. McComas, J. L. Phillips, V. J. Pizzo, and R. J. Forsyth, Ulysses observations of opposed tilts of solar wind corotating interaction regions in the northern and southern solar hemispheres, *Geophys. Res. Lett.*, **22**, 3333, 1995b.
- Gosling, J. T., S. J. Bane, W. C. Feldman, D. J. McComas, J. L. Phillips, B. E. Goldstein, M. Neugebauer, J. Burkepile, A. J. Hundhausen, and L. Acton, The band of solar wind

- variability at low heliographic latitudes near solar activity minimum: Plasma results from the Ulysses rapid latitude scan, *Geophys. Res. Lett.*, **22**, 3329, 1995c.
- Gosling, J. T., S. J. Bane, W. C. Feldman, D. J. McComas, P. Riley, B. E. Goldstein, and M. Neugebauer, The northern edge of the band of solar wind variability: Ulysses at ~ 4.5 AU, *Geophys. Res. Lett.*, **24**, 309, 1997.
- Jokipii, R. J., and B. Thomas, Effects of drift on the transport of cosmic rays. IV. Modulation by a wavy interplanetary current sheet, *Astrophys. J.*, **243**, 1115, 1981.
- Levine, R. J., M. D. Altschuler, and J. W. Harvey, Solar sources of the interplanetary magnetic field and solar wind, *J. Geophys. Res.*, **82**, 1061, 1977.
- Linker, J. A., and Z. Mikić, Extending coronal models to Earth orbit, in *Coronal mass ejections*, *Geophys. Monograph 99*, edited by N. Crooker, J. Joselyn, and J. Feynmann, American Geophysical Union, Washington, D.C., 269, 1997.
- Linker, J. A., Z. Mikić, D. A. Bisecker, R. J. Forsyth, S. E. Gibson, A. J. Lazarus, A. Lecinski, P. Riley, A. Szabo, and B. J. Thompson, Magnetohydrodynamic modeling of the solar corona during whole sun month, *J. Geophys. Res.*, **104**, 9809, 1999.
- Lionello, R., Z. Mikić, and J. A. Linker, Magnetohydrodynamics of solar coronal plasmas in cylindrical geometry, *J. Comput. Phys.*, **140**, 172, 1998.
- Lionello, R., J. A. Linker, and Z. Mikić, Including the transition region in models of the large-scale solar corona, to appear in *Astrophys. J.*, January, 2001.
- D. J. McComas, S. J. Bane, B. L. Barraclough, W. C. Feldman, H. O. Funsten, J. T. Gosling, P. Riley, R. Skoug, A. Balogh, R. J. Forsyth, B. E. Goldstein, and M. Neugebauer, Ulysses' return to the slow solar wind, *Geophys. Res. Lett.*, **25**, 1, 1998a.
- D. J. McComas, P. Riley, J. T. Gosling, A. Balogh, and R. J. Forsyth, Ulysses' rapid crossing of the polar coronal hole boundary, *J. Geophys. Res.*, **103**, 1955, 1998b.
- Mikić, Z., and J. A. Linker, Disruption of coronal magnetic field arcades, *Astrophys. J.*, **430**, 898, 1994.
- Mikić, Z., and Linker, J. A., The large-scale structure of the solar corona and inner heliosphere, in *Solar Wind Eight*, edited by D. Winterhalter, J. T. Gosling, S. R. Habbal, W. S. Kurth, and M. Neugebauer, published by American Institute of Physics, 1996.

- Mikić, Z., J. A. Linker, D. D. Schnack, R. Lionello, and A. Tarditi, Magnetohydrodynamic modeling of the global solar corona, *Phys. Plasmas*, **6**, 2217, 1999.
- Ogilvie, K. W., et al., A comprehensive plasma instrument for the WIND spacecraft, *Space Sci. Rev.*, **71**, 55, 1995.
- Pizzo, V. J., Interplanetary shocks on the large scale: A retrospective on the last decade's theoretical efforts, pp. 51-68, *Geophys. Monograph 35*, published by the American Geophysical Union, Washington, D. C., 1985.
- Pizzo, V. J., The evolution of corotating stream fronts near the ecliptic plane in the inner solar system, 2, Three-dimensional tilted-dipole fronts, *J. Geophys. Res.*, **96**, 5405, 1991.
- Pizzo, V. J., Global, quasi-steady dynamics of the distant solar wind, 1, Origin of north-south flows in the outer heliosphere, *J. Geophys. Res.*, **99**, 4173, 1994a.
- Pizzo, V. J., Global, quasi-steady dynamics of the distant solar wind, 2, Deformation of the heliospheric current sheet, *J. Geophys. Res.*, **99**, 4185, 1994b.
- Pizzo, V. J., and J. T. Gosling, 3-D simulation of high-latitude interaction regions: Comparison with Ulysses results, *Geophys. Res. Lett.*, **21**, 2063, 1994.
- Riley, P., J. T. Gosling, L. A. Weiss, and V. J. Pizzo, The tilts of corotating interaction regions at mid-heliographic latitudes, *J. Geophys. Res.*, **101**, 24,349, 1996.
- Sanderson, T. R., D. Lario, M. Maksimovic, R. G. Marsden, C. Tranquille, A. Balogh, R. J. Forsyth, and B. E. Goldstein, Current sheet control of recurrent particle increase at 4-5 AU, *Geophys. Res. Lett.*, **26**, 1785, 1999.
- Sarabhai, V., Some consequences of nonuniformity of solar wind velocity, *J. Geophys. Res.*, **68**, 1555, 1963.
- Smith, E. J., and J. H. Wolfe, Observations of interaction regions and corotating shocks between one and five AU: Pioneers 10 and 11, *J. Geophys. Res.*, **81**, 137, 1976.
- Smith, E. J., A. Balogh, M. E. Burton, G. Erdős, and R. J. Forsyth, Results of the Ulysses fast latitude scan: Magnetic field observations, *Geophys. Res. Lett.*, **22**, 3325, 1995.
- Totten, T. L., J. W. Freeman, and S. Arya, Application of the empirically derived polytropic index for the solar-wind to models of solar-wind propagation, *J. Geophys. Res.*, **101**, 15,629, 1996.

Tsurutani, B. T., and E. J. Smith, Interplanetary discontinuities: Temporal variations and radial gradient, *J. Geophys. Res.*, **84**, 2773, 1979.

Wang, Y. -M., and N. R. Sheeley, Jr., Solar wind speed and coronal flux-tube expansion, *Astrophys. J.*, **355**, 726, 1990.

Wang, Y. -M., and N. R. Sheeley, Jr., The high-latitude solar wind near sunspot maximum, *Geophys. Res. Lett.*, **24**, 3141, 1997.

J. A. Linker, Z. Mikić, and P. Riley, Science Applications International Corporation, San Diego, CA 92121. (e-mail:linker@iris023.saic.com; mikic@iris023.saic.com; uk2@haven.saic.com)

Received N/A; revised N/A; accepted N/A.

Figure 1. Figure 1: Derivation of the radial speed profile at $30R_s$: (a) Location of open and closed magnetic field lines in the photosphere; (b) Radial speed profile based on equation (7); and (c) Speed profile at $30R_s$.

Figure 2. Model solution for CR 1912-1913. The heliospheric current sheet (inferred from the iso-surface $B_r = 0$) is displayed out to 5 AU. The central sphere marks the inner boundary at $30R_s$. A meridional slice of the radial velocity is shown at an arbitrary longitude. Blue corresponds to slowest speeds ($\sim 350 \text{ km s}^{-1}$) and red corresponds to fastest speeds ($\sim 750 \text{ km s}^{-1}$). Superimposed is a selection of interplanetary magnetic field lines originating from different latitudes. Finally, the trajectories of the WIND and Ulysses spacecraft are marked.

Figure 3. Large-scale structure of the heliosphere in the meridional plane for the same interval as Figure 2. Left panel shows color contours of radial velocity, middle panel shows contours of number density (scaled by r^2), and right panel shows contours of gas, or thermal pressure (scaled by r^3) at an arbitrary longitude. In each panel, the location of the HCS is marked by the white curve.

Figure 4. From top left, in a clockwise direction: the radial velocity, meridional velocity, azimuthal velocity, scaled number density, thermal pressure, and magnetic field magnitude, at a heliocentric distance of 2.3 AU. In each panel, a black line marks the location of the HCS.

Figure 5. Comparison of Ulysses in situ measurements of speed, density, and temperature (squares) with simulation results (solid curves) for WSM time period.

Figure 6. Comparison of WIND in situ measurements of speed, density, and temperature (squares) with simulation results (solid curves) for WSM time period.

Figure 7. Comparison of Ulysses observations (blue) and simulation results (red) of speed, density, and temperature from September, 1994 to July, 1995.

Figure 8. (a) Speed profile in the photosphere for time period day 66-94, 1999, corresponding to CR 1947. (b) Inferred speed profile at $30 R_s$.

Figure 9. Meridional slices (at an arbitrary longitude) of radial velocity, scaled number density, and scaled thermal pressure for CR 1947. The white curves mark the location of the HCS.

Figure 10. Spherical slices of the three velocity components (top panels) and density, thermal pressure, and magnetic field magnitude (bottom panels) for CR 1947.

Figure 11. HCS at the three epochs of the solar cycle described in the text: (a) solar minimum; (b) the declining phase; and (c) approaching solar maximum.

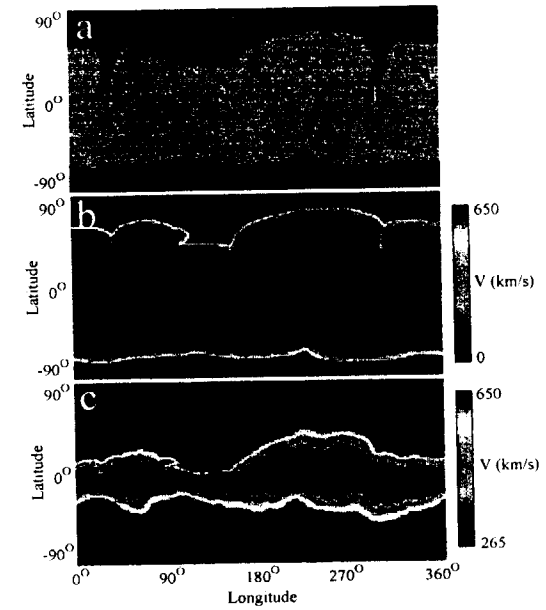


Figure 1

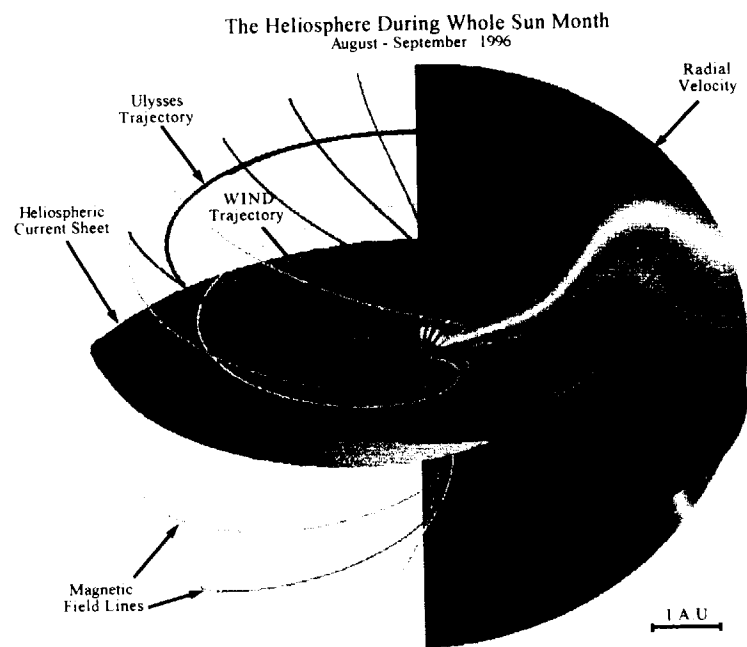


Figure 2

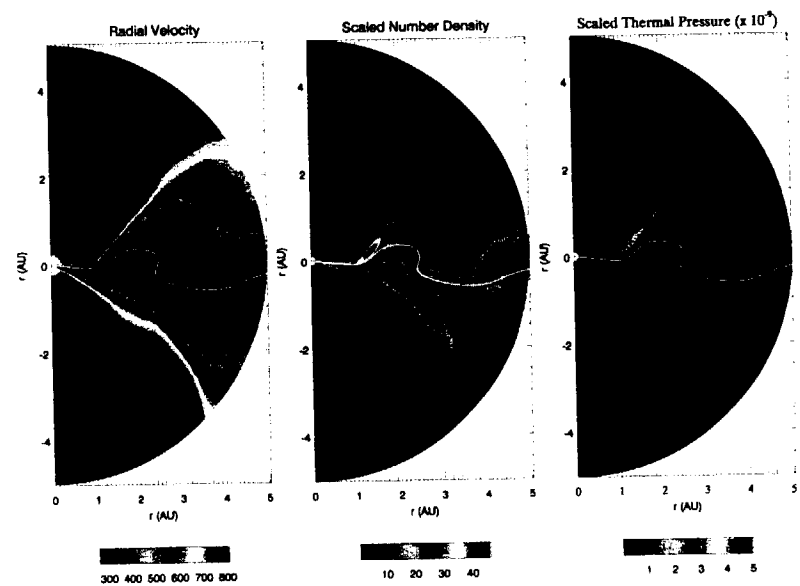


Figure 3

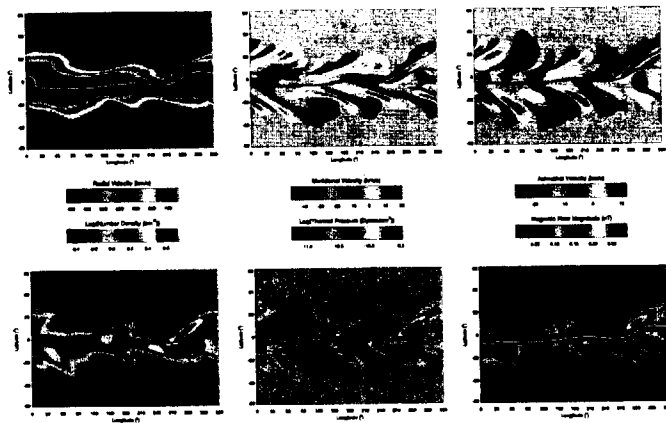


Figure 4

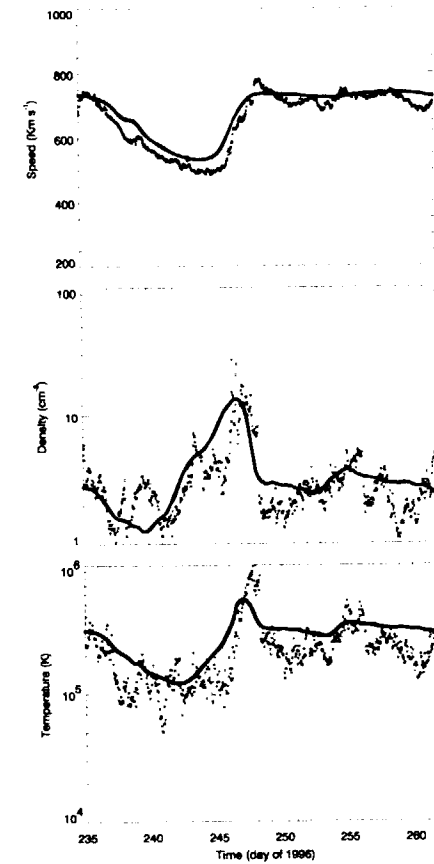


Figure 5

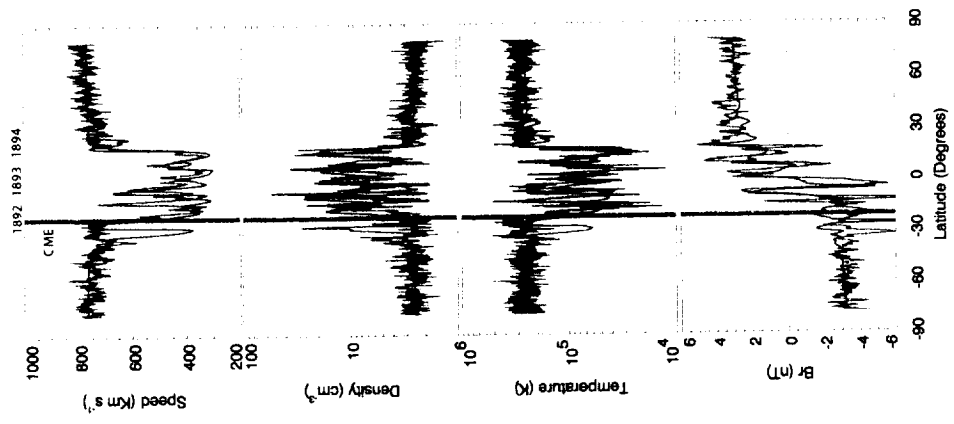


Figure 7

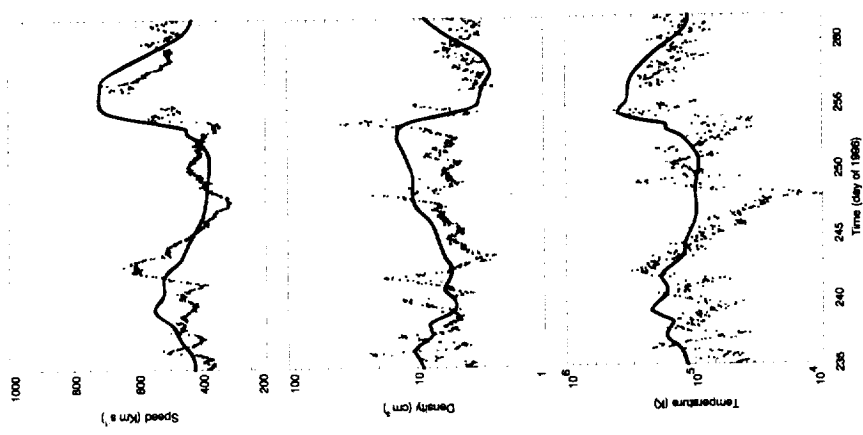


Figure 6

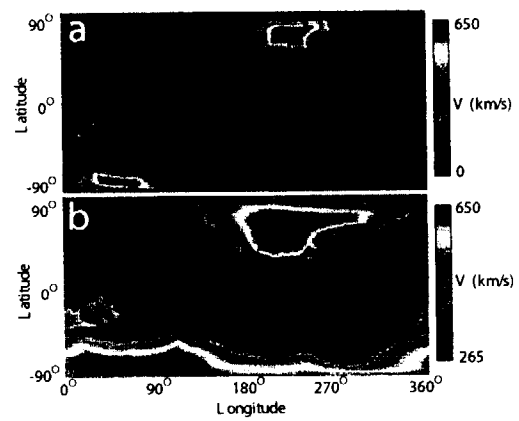


Figure 8

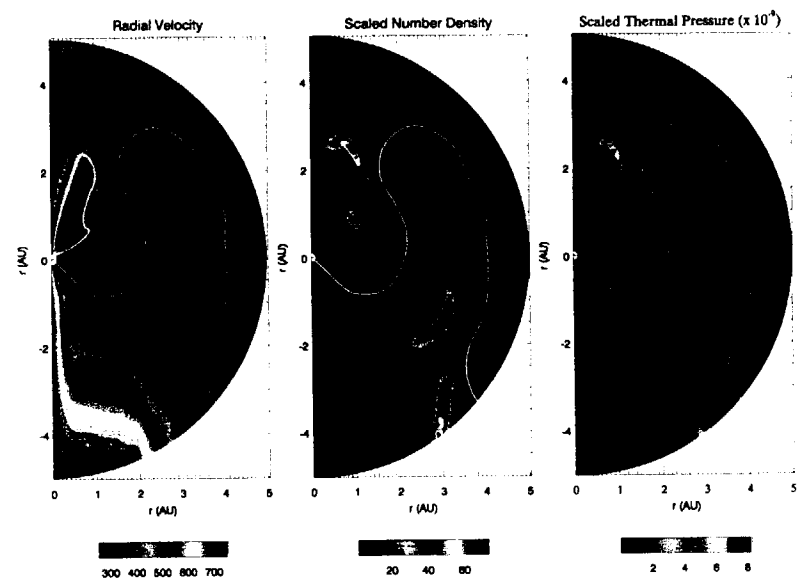


Figure 9

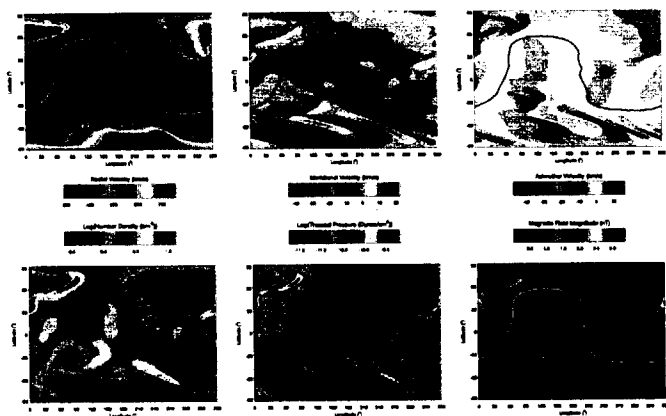


Figure 10

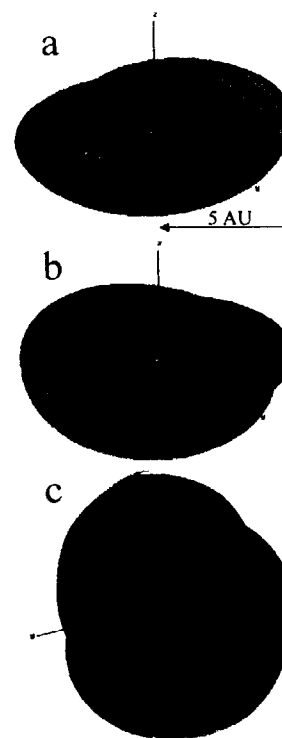


Figure 11

APPENDIX C

“Magnetohydrodynamic Modeling of Prominence Formation Within a Helmet Streamer”

J. A. Linker, R. Lionello, Z. Mikić, and T. Amari

Accepted for publication in *Journal of Geophysical Research*

Magnetohydrodynamic Modeling of Prominence Formation within a Helmet Streamer

J. A. Linker,¹ R. Lionello,¹ Z. Mikić,¹ and T. Amari²

Abstract. We present a 2.5D axisymmetric MHD model to self-consistently describe the formation of a stable prominence that supports cool, dense material in the lower corona. The upper chromosphere and transition region are included in the calculation. Reducing the magnetic flux along the neutral line of a sheared coronal arcade forms a magnetic field configuration with a flux-rope topology. The prominence forms when dense chromospheric material is brought up and condenses in the corona. The prominence sits at the base of a helmet streamer structure. The dense material is supported against gravity in the dips of the magnetic field lines in the flux rope. Further reduction in magnetic flux leads to an eruption of the prominence, ejecting material into the solar wind.

Short title: MAGNETOHYDRODYNAMIC MODELING OF PROMINENCES

1. Introduction

Prominences (called filaments when observed on the solar disk) support cool, dense chromospheric material ($\sim 10^4\text{K}$ and $10^{10} - 10^{11}/\text{cm}^3$) against the solar gravity in the surrounding hot, tenuous corona ($\sim 10^6\text{K}$ and $10^7 - 10^9/\text{cm}^3$). They are observed to lie above magnetic neutral lines in the photosphere and near the base of helmet streamers (regions of closed magnetic field that have confined the coronal plasma). The magnetic field in the prominence often exhibits "inverse polarity," meaning that when the coronal magnetic fields embedded in the prominence cross over the neutral line they point in the direction opposite to that indicated by the photospheric magnetic field polarity. The prominence magnetic field is itself nearly aligned with the filament channel [Martin *et al.*, 1994; Martin and Echols, 1994], indicating a highly sheared (and therefore magnetically energized) configuration.

Prominences have been studied for many years, yet the means by which these structures form and are maintained is still not understood, nor is their violent eruption. Three main difficulties confront any prospective theory attempting to describe the formation and evolution of prominences: (1) Finding a magnetic configuration with "dips" (concave upward portions of fluxtubes) that can gravitationally support the dense material; (2) understanding the mechanism by which chromospheric material is trapped in the dipped field lines and maintained there to form a condensation; (3) elucidating the process that leads to the release of magnetic energy and the disruption of these structures. Because of the great complexity of the entire problem, these three individual aspects have typically been approached separately.

Models of magnetic field configurations for prominence support that develop the required dips and inverse polarity usually compute force-free magnetic fields and assume that the prominence material provides only a small perturbation to the magnetic structure [e.g., van Ballegoijen and Martens, 1989, 1990; Antiochos *et al.*, 1994; Aulanier and Demoulin, 1998; Amari *et al.*, 1999]. Given a favorable structure for

supporting the filament, computation of the complicated dynamics and thermodynamics of condensations have been performed by assuming that the plasma flows along fixed magnetic flux tubes, which reduces the problem to one-dimensional hydrodynamics with energy transport [Poland and Mariska, 1986; Mok *et al.*, 1990; Antiochos and Klimchuk, 1991; Antiochos *et al.*, 1999a].

Models of prominence eruption typically start from configurations favorable for prominence support [e.g., van Ballegoijen and Martens, 1989; Priest and Forbes, 1990; Isenberg *et al.*, 1993] and are closely related to the problem of coronal mass ejection (CME) initiation [Forbes and Priest, 1995; Linker and Mikić, 1995; Low, 1997; Mikić and Linker, 1997; Wu and Guo, 1997; Antiochos *et al.*, 1999b; Lin and Forbes, 2000], as these phenomena are linked observationally [Hundhausen, 1997] and require the release of stored magnetic field energy and the opening of previously closed magnetic field regions [e.g., Aly, 1984; Sturrock, 1991; Forbes, 1992; Mikić and Linker, 1994; Antiochos, 1998]. In recent simulations [Mikić *et al.*, 1999; Amari *et al.*, 1999, 2000] we have found that magnetic flux emergence and cancellation in the photosphere can lead to the formation of magnetic flux ropes in sheared or twisted arcade configurations. When the flux cancellation reaches a critical threshold, the entire configuration erupts with a considerable release of magnetic energy.

The theoretical investigations described above decouple the salient processes and focus on modeling individual aspects of the problem. This approach is useful for revealing the basic underlying physics. However, a complete picture of prominence formation, evolution, and eruption ultimately requires a comprehensive model of all of the processes together. This is particularly true now that different models can more or less equally describe the basic features of the observations, albeit somewhat superficially. Eventually, models will need to produce more detailed predictions that can be tested directly by observations (for example, by producing simulated emission that can be compared with images from spacecraft such as SOHO or TRACE). This challenging

goal requires that the complex thermodynamic processes of the upper chromosphere and transition region be incorporated into multi-dimensional magnetohydrodynamic (MHD) computations.

The purpose of this paper is to demonstrate that we can now begin to study the problem of prominence formation and eruption with a more comprehensive approach. We show that when energy transport processes are included into calculations similar to our recent models of prominence support and eruption, chromospheric-like material can be trapped on helical field lines and lifted into a stable configuration in the lower corona as a result of flux cancellation at the neutral line. When further flux cancellation occurs, the entire configuration erupts into the corona.

The plan for the rest of the paper is as follows: In the next section (2), we describe our computational methodology. Section 3 describes results for both polytropic and full thermodynamic simulations, and section 4 discusses the implications of our work and directions for future progress.

2. Methodology

Lionello et al. [1999a; 2001] describe the use of our time-dependent 3D MHD model to compute helmet streamer configurations in the solar corona that include the lower solar atmosphere (upper chromosphere and transition region). Those calculations form the basis for the studies discussed in this paper; here we note some important details relevant to the present calculations.

In this paper we confine ourselves to azimuthally symmetric, two-dimensional solutions (with three components of magnetic field and velocity). We solve the following set of equations in spherical coordinates:

$$\nabla \times \mathbf{B} = \frac{4\pi}{c} \mathbf{J}, \quad (1)$$

$$\frac{1}{c} \frac{\partial \mathbf{B}}{\partial t} = -\nabla \times \mathbf{E}, \quad (2)$$

$$\mathbf{E} + \frac{1}{c} \mathbf{v} \times \mathbf{B} = \eta \mathbf{J}, \quad (3)$$

$$\frac{\partial \rho}{\partial t} + \nabla \cdot (\rho \mathbf{v}) = 0, \quad (4)$$

$$\frac{1}{\gamma - 1} \left(\frac{\partial T}{\partial t} + \mathbf{v} \cdot \nabla T \right) = -T \nabla \cdot \mathbf{v} - \frac{m}{k\rho} (\nabla \cdot \mathbf{q} + n_e n_p Q(T) - H_{\text{ch}} - H_\eta - H_\nu), \quad (5)$$

$$\rho \left(\frac{\partial \mathbf{v}}{\partial t} + \mathbf{v} \cdot \nabla \mathbf{v} \right) = \frac{1}{c} \mathbf{J} \times \mathbf{B} - \nabla \mathbf{p} + \rho \mathbf{g} + \nabla \cdot (\nu \rho \nabla \mathbf{v}), \quad (6)$$

where \mathbf{B} is the magnetic field, \mathbf{J} is the electric current density, \mathbf{E} is the electric field, ρ , \mathbf{v} , p , and T are the plasma mass density, velocity, pressure, and temperature, $\mathbf{g} = -g_0 \hat{\mathbf{r}} R_s^2 / r^2$ is the gravitational acceleration (with R_s the solar radius), η the resistivity, and ν is the kinematic viscosity. In the energy equation, Eq. (5), $Q(T)$ is the (optically thin) radiation loss function as in *Athay* [1986], n_e and n_p are the electron and proton number density (which are equal for a hydrogen plasma), $\gamma = 5/3$ is the polytropic index, H_{ch} is the coronal heating term (a parameterized function), $H_\eta = \eta J^2$ and $H_\nu = \rho \nu \nabla \mathbf{v} : \nabla \mathbf{v}$ are the ohmic and viscous heating terms (neglected in these simulations), and \mathbf{q} is the heat flux.

Coronal heating is specified as a nonuniform profile that varies exponentially with radial distance, and both the heat deposition length scale (λ) and flux vary with latitude. The length scale varies from $\lambda = 0.7 R_s$ at the poles to $\lambda = 0.1 R_s$ at the equator, and the heat flux at $r = R_s$ is $10^5 \text{ erg cm}^{-2} \text{ s}^{-1}$ at the poles and $5 \times 10^5 \text{ erg cm}^{-2} \text{ s}^{-1}$ at the equator. These parameters have been chosen to yield the strongly concentrated heating and higher densities seen in active regions near the equator of the simulation while also providing the more distributed heating present in coronal holes in the open field portions of the simulation. *Lionello et al.* [2001] describes further details of the coronal heating parameters and the use of both collisional (Spitzer's law) and collisionless [*Hollweg*, 1978] thermal conduction as a function of radial distance from the Sun. For the results shown in this paper, we have modified the Spitzer law to reduce the steepness of the temperature and density gradients in the lowest part of the transition

region (see the Appendix for a more detailed discussion). We have found that this procedure allows coarser meshes to be used and yields solutions that are qualitatively similar to those obtained with the full Spitzer thermal conductivity.

The calculation described here has been performed on a 201×201 nonuniform (r, θ) grid, with the mesh points highly concentrated in the equatorial region near the lower boundary. A mesh with $\Delta r \approx 6 \times 10^{-4} R_s$ in the upper chromosphere (near the lower radial boundary) and $\Delta \theta \approx 0.2^\circ$ near the equator is used. Other calculations with 121×101 mesh points, with coarser mesh resolution, were also performed prior to this calculation in order to scope out the parameters and find a regime in which a prominence was formed. The results with the higher-resolution mesh allowed us to use a larger Lundquist number, and we report only these results here. This simulation used 20 hours of CPU time on a Cray T90 supercomputer, and we did not deem it necessary to pursue calculations with higher mesh resolution considering the limitations on our computing resources. We believe that increasing the resolution beyond that used in the present calculation would not change the results significantly. However, when we begin modeling more realistic prominences in the future we will verify that a further increase in the spatial resolution does not change the results.

The simulation domain extends out to $30R_s$. At this upper boundary the flow is supersonic and super-Alfvénic, and we implement boundary conditions that utilize the characteristics to allow only outgoing waves there [Linker and Mikić, 1997]. A uniform resistivity η has been used, corresponding to a resistive diffusion time $\tau_R = 4\pi R_s^2 / (\eta c^2) = 4 \times 10^4$ hours (for a length scale of R_s). Underneath the relaxed helmet streamer, the Alfvén speed (V_{A0}) near the equator at 10,000–20,000 km altitude is about 1830 km/s, so the Alfvén travel time ($\tau_A = R_s / V_{A0}$) is 6.3 minutes, and the Lundquist number $\tau_R / \tau_A \approx 3.8 \times 10^5$. A uniform viscosity ν is also used, corresponding to a viscous diffusion time $\tau_\nu = R_s^2 / \nu$ such that $\tau_\nu / \tau_A = 3.8 \times 10^3$. Typically, we find that much higher values of τ_R can be specified for our algorithm if τ_ν is kept at a

relatively smaller value.

The method of solution of (1-6) has been described previously [Mikić and Linker, 1994; Linker and Mikić, 1997; Lionello et al. 1999b; Linker et al. 1999; Mikić et al. 1999]. For the parameter regime of the calculations we describe here, stiffness of the equations is introduced by the combination of both the high Alfvén speed and thermal conduction in the transition region and lower corona, and the use of small mesh cells in this region to capture the steep gradients in density and temperature there. The stiffness introduced in the time-integration of the equations by the Alfvén speed is treated efficiently using a semi-implicit method [Mikić and Linker, 1994]. The accuracy of the semi-implicit method has been studied previously [Schmuck et al., 1987; Mikić et al., 1988], and it is known that when the time step falls below the CFL limit, the semi-implicit method is identical to an explicit method. The stiffness introduced by the parabolic equations resulting from the thermal conduction, resistivity, and viscosity, are treated using standard fully-implicit methods.

3. Results

Amari et al. [1999; 2000] have described how magnetic flux changes at the photosphere, when introduced into a three-dimensional sheared arcade field, can yield solutions with stable magnetic flux ropes suitable for prominence support, and how further magnetic flux changes can lead to magnetic energy release and eruption. These calculations were performed in the “zero beta” limit of equations (1-6): equations (1-3) and (6) are solved with $P = 0$ and a fixed profile assumed for ρ (equilibria found in this manner are force-free solutions). Mikić and Linker [1999] have shown that when the same procedure is applied to polytropic MHD solutions with helmet streamer configurations [solutions of equations (1-6) with the energy source terms in (5) set to zero and $\gamma = 1.05$], the streamer disrupts and material is ejected out into the solar wind. Figure 1 shows the eruption of a flux rope in a three-dimensional calculation of this kind.

A detailed description of these results is presently in preparation. Here we describe how the inclusion of processes in the lower solar atmosphere in these calculations [full solutions of equations (1-6)] leads to the formation of a prominence-like structure and its subsequent eruption.

3.1. Helmet Streamer Solution

In the first phase of the calculation, we generate a helmet streamer equilibrium [e.g., *Linker and Mikić, 1995*]. We start with a potential magnetic field in the corona that matches a specified distribution of radial magnetic field at the solar surface B_{r0} . The distribution we choose is the sum of a weak dipole field ($B_{\text{odip}} = 2.2\text{G}$ at the poles), and a stronger ($B_{\text{obip}} = 9.5\text{G}$) concentrated bipole near the neutral line. For simplicity we choose a configuration that is symmetric in latitude about the solar equator. Our intent in including the strong bipole is to model the large-scale effect of the field in an active region (where prominences frequently form). The equatorial position of the bipole at the equator is not very realistic for prominences, but is convenient for the illustrative purposes of this calculation. We place our lower boundary at the top of the chromosphere, and we impose a fixed temperature $T_0 = 20,000\text{K}$ and a plasma number density $n = n_p = n_e = 10^{11}\text{cm}^{-3}$. We impose a spherically symmetric solar wind solution which includes the upper chromosphere and the transition region and is consistent with the chosen boundary values for temperature and density. This combination is not initially at equilibrium. We integrate the time-dependent MHD equations in time until the solution settles down to an equilibrium (for $380\tau_A$, where τ_A is the Alfvén time described in section 2). The final state models the coronal plasma, and includes the transition region in the calculation. This procedure has been described by *Lionello et al. [2001]*. The final solution has a coronal streamer with closed field lines, surrounded by open field lines along which the solar wind flows outward. Figure 1 of *Linker and Mikić [1995]* shows an example of the magnetic configuration of a 2D helmet streamer

using a polytropic energy equation: Figure 1 and Figure 3 of *Lionello et al. [2001]* show examples of a helmet streamer configuration computed with thermodynamics.

3.2. An Energized Helmet Streamer

In the second phase of the simulation, we apply a shear flow near the neutral line that builds free magnetic energy into the streamer. This shear flow is not intended to model actual flows on the Sun. It is just a convenient mechanism for producing strongly sheared field lines that are nearly aligned with the neutral line, a frequently observed characteristic of filaments [*Martin and Echols, 1994*]. We use a shear profile that is like the one used by *Mikić and Linker [1994]*, with a width $\Delta\theta_m = 8.5^\circ$. The shear is applied from $t = 380\tau_A$ to $t = 570\tau_A$, with a maximum velocity $v_0 = 0.005V_{A0}$. Figure 2a and 3a show contours of the flux function (projections of the magnetic field lines) superimposed on the plasma density (Figure 2a) and plasma temperature (Figure 3a), at the end of the shearing phase. The maximum displacement of the footpoints from their original position is $0.8R_s$, and the sheared field has a magnetic energy equal to $2.3W'_{pot}$. The calculation is then continued in a relaxation phase to $t = 589\tau_A$.

3.3. Creation of a Magnetic Flux Rope and Subsequent Eruption

In the final phase of the calculation, we change the magnetic flux at the boundary to generate a flux rope. On the Sun it is frequently observed that the magnetic fields in an active region tend to disperse days to weeks after its emergence. During this time, filaments are frequently observed to form along the neutral line. At times, these filaments disappear, presumably due to eruption, and may even reform in the same location later. This dispersal of magnetic flux is thought to occur on a small spatial scale by annihilation and submergence of magnetic dipole elements, and has been modeled as a convective-diffusive process on a large scale [*Wang et al., 1989; Wang and Sheeley, 1990*]. The disappearance of photospheric magnetic flux has long been suspected of

playing a role in filament formation and eruption [van Ballegoijen and Martens, 1989]. We model the effect of such changes by reducing the magnetic flux in the bipolar flux region. The electric fields that specify this change (described below) imply converging flows at the neutral line, as is believed to occur in flux cancellation. We find that the reduction in magnetic flux can create a filament, and that further reduction in flux can make it erupt, as illustrated below.

The boundary conditions for flux reduction are essentially the same as those described by Amari *et al.* [2000]. The change in flux is applied by specifying the appropriate electric fields at the boundary. For example, when we seek steady-state solutions of eqs. (1-6), we set the tangential component of the electric field at the boundary, (\mathbf{E}_{t0}), to zero. This keeps B_{r0} (the radial magnetic field at the solar boundary) fixed in time. In order to specify a desired change in the magnetic flux, we specify a non-zero \mathbf{E}_{t0} that is consistent with the required $\partial B_{r0}/\partial t$. Reduction of B_{r0} is equivalent to cancellation of flux at the neutral line, and leads to the formation of a flux rope [Amari *et al.* 2000].

To compute the electric field required to drive a specific flux change, we note that in general, \mathbf{E}_{t0} can be expressed as $\nabla \times \psi \hat{r} + \nabla_t \phi$, where ψ and ϕ are arbitrary functions (of θ and ϕ) and ∇_t indicates transverse derivatives (in the $\theta - \phi$ plane at $r = R_s$). The potential ϕ changes \mathbf{E}_{t0} without changing B_{r0} , and can be used to control the transverse magnetic field (i.e., the shear and the normal electric current), whereas the potential ψ changes the flux. For the simulation presented in this paper we used $\phi = 0$, which minimizes changes to B_ϕ . Then $c\nabla_t^2 \psi = \partial B_{r0}/\partial t$, which can be solved for ψ for the flux change specified by $\partial B_{r0}/\partial t$.

For the case presented here, we apply the appropriate electric field \mathbf{E}_{t0} at the lower boundary, as calculated above, to reduce the bipole portion of the flux distribution B_{r0bip} by 15% (while leaving the dipole portion B_{r0dip} undisturbed), from $t = 589\tau_A$ to $665\tau_A$. Figure 2 shows the resulting evolution of the plasma density and projected

magnetic field lines (for a portion of the simulation); Figure 3 shows the corresponding evolution of the plasma temperature. At $t = 608\tau_A$ when the flux has been reduced by 3.75% (Figure 2b and 3b), a flux rope containing cold dense chromospheric material ($T = 2 \times 10^4$ and $n > 10^{10}$) has been lifted into the corona to form a prominence-like structure (barely visible near the lower boundary at the equator). In a detailed analysis of vector magnetograph and H α observations of an emerging δ -sunspot group, Lites *et al.* [1995] suggested that a twisted magnetic loop emerged from below the photosphere, carrying with it dense material that formed a filament. The filament-formation mechanism we describe is consistent with these observations. This is in contrast to the idea of siphon flows leading to the development of a condensation [e.g. Antiochos *et al.*, 1999a], which cannot occur here because the flux rope field lines do not connect to the surface.

At $t = 646\tau_A$ shown in Figure 2c and 3c (flux reduction at 11.25%) the prominence has already begun to erupt. It has been lifted to a height of $0.2R_s$ (140,000 km) and is slowly moving upward. By $t = 684\tau_A$ ($19\tau_A$ after flux reduction was halted) the flux rope and helmet streamer are erupting (Figures 2d and 3d), and the entire configuration is opened and material is carried upward (Figures 2e and 3e).

There is a threshold of flux reduction for the eruption to occur. To demonstrate this behavior, we performed another case where flux reduction is halted at $t = 608\tau_A$ ($= 3.75\%$ of the initial amount). When the calculation is continued from that point, no eruption occurs and the flux rope containing chromospheric material relaxes to a stable state. Figure 4 shows a closeup of this configuration after it has relaxed for $19\tau_A$. On the left are shown projected field lines overlaid on the plasma density (Figure 4a) and temperature (Figure 4b). Note the presence of high density and low temperature on the detached flux surfaces. On the right, field lines from the calculation are plotted with the color along the field line indicating the density (Figure 4c) and temperature (Figure 4d). Cool and dense material in the prominence is supported against gravity in the dips of

the field lines of the flux rope. The height of the simulated prominence is about 15,000 km. As the calculation is continued further, the flux rope slowly diffuses because of the presence of finite resistivity.

If flux reduction is halted at a level of 7.5% of the initial amount and the calculation is continued, the flux rope and helmet streamer erupt in a manner similar to the case shown in Figure 2-3. We have found that the exact level of flux reduction necessary for eruption in a given configuration depends on the details of the surface flux distribution and the amount of shear introduced. Prior to reaching the critical level, the behavior of the system is quasistatic.

Figure 5 shows the prominence height as a function of time during the eruptive phase. The eruption that was produced in this case was not very fast (reaching $\approx 40\text{km/s}$ at $2R_s$), although it is still accelerating at this stage. This is in contrast to some of the polytropic simulations we have run with this mechanism (speeds $> 500\text{km/s}$). A more concentrated shear and a larger initial magnetic field strength (enabling release of more magnetic energy) may be required to create a fast mass ejection containing a filament.

4. Discussion

The possibility that prominences are supported by magnetic flux ropes has been considered in recent years by a number of authors [e.g. *van Ballegoijen and Martens*, 1989, 1990; *Rust and Kumar*, 1994; *Chen*, 1996; *Aulanier and Demoulin*, 1998]. Our recent work [*Amari et al.* 1999, 2000] and the results we have presented here are similar in many respects to the force-free calculations of *van Ballegoijen and Martens* [1989], which showed how flux cancellation could lead to the formation of flux ropes. The computations we have described here show that when the full MHD equations are used, including an energy equation that takes into account energy transport in the upper chromosphere and transition region, chromospheric material can be lifted by the helical field lines and supported against gravity inside a helmet streamer. The flux rope can

subsequently be ejected into the solar wind as a consequence of eruption.

The idealized calculations presented here are intended to illustrate that it is possible to perform self-consistent MHD calculations of prominences. Clearly, a 2D axisymmetric model has limited applicability to solar observations. In this geometry the helical field lines of the flux rope form a torus around the Sun. The connection of the magnetic fields embedded in the prominence to the photosphere, and the possible role of siphon flows in filling/draining the prominence, is an important question not addressed by this calculation. Preliminary one-dimensional solutions for energy flow along the magnetic field loops from a three-dimensional flux-rope configuration indicate that condensations do indeed form, but a fully self-consistent 3D simulation is required to investigate this question more completely. We have performed 3D simulations of flux-rope formation in polytropic helmet streamers (Figure 1), and we intend to extend the present results to 3D as well.

Once the simulations become more realistic, it will be necessary to explain the many detailed features that have been observed in prominences [e.g. *Martin et al.* 1994]. For example, what are the implications of the observed relationship between the filament axial field and the skew of coronal arcades [*Martin and McAllister*, 1996], and the relationship between differential solar rotation and the axial field in polar crown filaments [*van Ballegoijen et al.* 1998]? Do these considerations imply that the axial field originates from below the photosphere [*Priest et al.* 1996]? Magnetic flux ropes are not the only candidates for explaining prominence support [*Martin and Echols*, 1994; *Antiochos et al.* 1994] and eruption [*Antiochos et al.* 1999b]. Understanding the pre-eruptive state of filaments, as well as their violent eruption, requires calculations that can predict observable quantities. We consider the calculations we have presented here as a first step of that process.

Appendix: Modified Thermal Conduction

In the lower transition region, there is a close balance between thermally conducted heat [$\nabla \cdot \mathbf{q}$ in equation (5)] coming from the hot, tenuous corona and the energy radiated away [$n_e n_p Q(T)$ in (5)] by the ambient dense cold material. In this collisional regime, the Spitzer form of the thermal conductivity is appropriate:

$$\mathbf{q} = -\kappa_{\parallel} \hat{\mathbf{b}} \hat{\mathbf{b}} \cdot \nabla T, \quad (\text{A1})$$

where $\kappa_{\parallel} = \kappa_0 T^{5/2}$ ($\kappa_0 = 9 \times 10^7$ in c.g.s. units), $\hat{\mathbf{b}}$ is the unit vector along the magnetic field, and T is the temperature in K.

The steepness of the temperature in the transition region arises from the balance of conductive heat flux from the corona and radiative losses in the transition region. The temperature dependence of the Spitzer thermal conductivity ($\kappa_{\parallel} \propto T^{5/2}$) forms the steepest temperature gradient in the lower transition region. *Lionello et al.* [2001] used highly resolved meshes ($\Delta r \approx 8 \times 10^{-5} R_{\odot}$, or 56 km) to capture this gradient. It seems that an artificial broadening of this gradient should be possible without qualitatively changing the overall solution. With this goal in mind, we have formulated κ_{\parallel} in such a way as to preserve the essential physics of the Spitzer model for the upper transition region and corona, while reducing the steepness of the gradient in the lower part of the transition region:

$$\kappa_{\parallel} = \kappa_0 \left[s T^{5/2} + (1-s) T^{\alpha} T_{\text{mod}}^{5/2-\alpha} \right], \quad (\text{A2})$$

where

$$s(T) = \frac{1}{2} \left(1 + \tanh \left(\frac{T - T_{\text{mod}}}{\Delta T_{\text{mod}}} \right) \right). \quad (\text{A3})$$

The function s varies smoothly between 0 and 1 and regulates the transition from the Spitzer regime of κ_{\parallel} (when $T \gtrsim T_{\text{mod}}$), and the modified regime (when $T \lesssim T_{\text{mod}}$). In the modified regime, which applies to the lower transition region, $\kappa_{\parallel} \propto T^{\alpha}$, and

the α power is $0 \leq \alpha \leq 5/2$. The transition between the two regimes occurs in a temperature interval depending on ΔT_{mod} . For the simulation results presented here, we chose $\alpha = 0$ (corresponding to constant κ_{\parallel} for $T \leq T_{\text{mod}}$), $T_{\text{mod}} = 250,000$ K, and $\Delta T_{\text{mod}} = 20,000$ K.

This formulation makes κ_{\parallel} higher than the Spitzer value in the lower transition region, allowing thermal conduction to balance radiation loss with a smaller temperature gradient. We have found that this modified form of the thermal conduction yields solutions that are qualitatively similar to those obtained with the full Spitzer thermal conductivity, and we were able to increase the radial grid size in the lower transition region by almost an order of magnitude over that used in *Lionello et al.* [2001]. Quantitatively, the temperature of solutions on individual loops matches closely in the corona, although differences in the density can be as large as a factor of two different. We regard the modified thermal conduction as a useful tool for exploring the qualitative properties of solutions without using extremely fine meshes.

Acknowledgments. These results were presented at the International Conference on Solar Eruptive Events, March 6-9, 2000, at the Catholic University of America. This work was supported by the NASA Sun Earth Connections Theory Program, the NASA Supporting Research and Technology program, and the NSF Space Weather program (jointly funded by NSF and AFOSR). Computations were at the San Diego Supercomputer Center (SDSC) and the National Energy Research Supercomputer Center (NERSC).

References

- Aly, J. J., On some properties of force-free magnetic fields in infinite regions of space. *Astrophys. J.*, 283, 349, 1994.
- Antiochos, S. K., The magnetic topology of solar eruptions. *Astrophys. J.*, 502, L181, 1998.
- Antiochos, S. K., R. B. Dahlburg, and J. A. Klimchuk, The magnetic field of solar prominences. *Astrophys. J.*, 420, L41, 1994.
- Antiochos, S. K., C. R. DeVore, and J. A. Klimchuk, A model for solar coronal mass ejections. *Astrophys. J.*, 510, 485, 1999b.
- Antiochos, S. K., and J. A. Klimchuk, A model for the formation of solar prominences. *Astrophys. J.*, 378, p. 372, 1991.
- Antiochos, S. K., P. J. MacNeice, D. S. Spicer, and J. A. Klimchuk, The dynamic formation of prominence condensations. *Astrophys. J.*, 512, 985, 1999a.
- Amari, T., J. F. Luciani, Z. Mikić, and J. A. Linker, Three-dimensional solutions of magnetohydrodynamic equations for prominence magnetic support: twisted magnetic flux rope. *Astrophys. J.*, 518, L57, 1999.
- Amari, T., J. F. Luciani, Z. Mikić, and J. A. Linker, A twisted flux rope model for coronal mass ejections and two-ribbon flares. *Astrophys. J.*, 529, L49, 2000.
- Athay, R. G., Radiation loss rates in Lyman-alpha for solar conditions. *Astrophys. J.*, 308, 975, 1986.
- Aulanier, G., and P. Demoulin, 3-D magnetic configurations supporting prominences. I. The natural presence of lateral feet. *Astronom. Astrophys.*, 329, 1125, 1998.
- Chen, J., Theory of prominence eruption and propagation: Interplanetary consequences. *J. Geophys. Res.*, 101, 27499, 1996.
- Forbes, T. G., and E. R. Priest, Photospheric magnetic field evolution and eruptive flares. *Astrophys. J.*, 446, 377, 1985.
- Hollweg, J. V., Some physical processes in the solar wind. *Rev. Geophys.*, 16, 689, 1978.
- Hundhausen, A. J., An introduction, in *Coronal Mass Ejections, Geophys. Monogr. Ser.*, edited by N. Crooker, J. A. Joselyn, and J. Feynman, 99, 1, AGU, Washington, 1997.
- Isenberg, P. A., T. G. Forbes, and P. Demoulin, Catastrophic evolution of a force-free flux rope: a model for eruptive flares. *Astrophys. J.*, 417, 368, 1993.
- Lin, J., and T. G. Forbes, Effects of reconnection on the coronal mass ejection process. *J. Geophys. Res.*, 105, 2375, 2000.
- Linker, J. A., and Z. Mikić, Disruption of a helmet streamer by photospheric shear. *Astrophys. J.*, 438, L45, 1995.
- Linker, J. A., and Z. Mikić, Extending coronal models to Earth orbit, in *Coronal Mass Ejections, Geophys. Monogr. Ser.*, edited by N. Crooker, J. A. Joselyn, and J. Feynman, 99, 269, AGU, Washington, 1997.
- Linker, J. A., Z. Mikić, D. A. Biesecker, R. J. Forsyth, S. E. Gibson, A. J. Lazarus, P. Riley, A. Szabo, and B. J. Thompson, Magnetohydrodynamic modeling of the solar corona during Whole Sun Month, *J. Geophys. Res.*, 104, 9809, 1999.
- Lionello, R., J. A. Linker, and Z. Mikić, Magnetohydrodynamics of the solar corona and transition region, in *Proceedings of 9th European meeting on Solar Physics, "Magnetic Fields and Solar Processes."* (A. Wilson ed.), p. 1181, ESA Publications Division, Noordwijk, 1999a.
- Lionello, R., Z. Mikić, and J. A. Linker, Stability of algorithms for waves with large flows. *J. Comput. Phys.*, 152, 346, 1999b.
- Lionello, R., J. A. Linker, and Z. Mikić, Including the transition region in models of the large-scale solar corona. *Astrophys. J.*, in press, 2001.
- Lites, B. W., B. C. Low, V. Martinez Pillet, P. Seagraves, A. Skumanich, Z. A. Frank, R. A. Shine, and S. Tsuneta, The possible ascent of a closed magnetic system through the photosphere. *Astrophys. J.*, 446, 877, 1995.
- Low, B. C., The role of coronal mass ejections in solar activity, in *Coronal Mass Ejections, Geophys. Monogr. Ser.*, edited by N. Crooker, J. A. Joselyn, and J. Feynman, 99, 39, AGU, Washington, 1997.
- Martin, S. F., and C. R. Echols, An observational and conceptual model of the magnetic field in solar prominences, in *Solar Surface Magnetism*, edited by R. J. Rutten and C. J. Schrijver, 339, Kluwer Academic, Dordrecht, Netherlands, 1994.

- Martin, S. F., R. Bilimoria, and P. W. Tracadas. Magnetic field configurations basic to filament channels and filaments, in *Solar Surface Magnetism*, edited by R. J. Rutten and C. J. Schrijver, 303. Kluwer Academic, Dordrecht, Netherlands, 1994.
- Martin, S. F., and McAllister, A. H., The skew of X-ray coronal loops overlying H alpha filaments, in *Magnetodynamic Phenomena in the Solar Atmosphere: Prototypes of Stellar Magnetic Activity*, edited by Y. Uchida, T. Kosugi, and H. S. Hudson, *IAU Colloq. 133*, 497. Kluwer Academic, Dordrecht, Netherlands, 1994.
- Mikić, Z., and J. A. Linker. Disruption of coronal magnetic field arcades, *Astrophys. J.*, **430**, 898, 1994.
- Mikić, Z., and J. A. Linker. The initiation of coronal mass ejections by magnetic shear, in *Coronal Mass Ejections, Geophys. Monogr. Ser.*, edited by N. Crooker, J. A. Joselyn, and J. Feynman, **99**, 57. AGU, Washington, 1997.
- Mikić, Z., and J. A. Linker. Initiation of coronal mass ejections by changes in photospheric flux, (abstract) *BAAAS*, **31**, 918, 1999.
- Mikić, Z., J. A. Linker, D. D. Schnack, R. Lionello, and A. Tarditi. Magnetohydrodynamic modeling of the global corona, *Phys. Plasmas*, **6**, 2217, 1999.
- Mok, Y., D. D. Schnack, and G. Van Hoven. The thermal stability of coronal loops - Numerical simulation, *Sol. Phys.*, **132**, 95, 1991.
- Poland, A. I. and J. T. Mariska. A siphon mechanism for supplying prominence mass, *Sol. Phys.*, **104**, 303, 1986.
- Priest, E. R., and T. G. Forbes. Magnetic field evolution during prominence eruptions and two-ribbon flares, *Sol. Phys.*, **126**, 319, 1990.
- Priest, E. R., A. A. van Ballegoijen, and D. H. Mackay. A model for dextral and sinistral prominences, *Astrophys. J.*, **460**, 530, 1996.
- Rust, D. M., and A. Kumar. Helical magnetic fields in filaments, *Sol. Phys.*, **155**, 69, 1994.
- Sturrock, P. A., Maximum energy of semi-infinite magnetic field configurations, *Astrophys. J.*, **380**, 655, 1991.
- van Ballegoijen, A. A., N. P. Cartledge, and E. R. Priest. Magnetic flux transport and the formation of filament channels on the Sun, *Astrophys. J.*, **501**, 866, 1998.

- van Ballegoijen, A. A., and P. C. H. Martens. Formation and eruption of solar prominences, *Astrophys. J.*, **343**, 971, 1989.
- van Ballegoijen, A. A., and P. C. H. Martens. Magnetic fields in quiescent prominences, *Astrophys. J.*, **361**, 283, 1990.
- Wang, Y.-M., A. G. Nash, and N. R. Sheeley, Jr., Magnetic flux transport on the sun, *Science*, **245**, 712, 1989.
- Wang, Y.-M., and N. R. Sheeley, Jr., Magnetic flux transport and the sunspot-cycle evolution of coronal holes and their wind streams, *Astrophys. J.*, **365**, 372, 1990.
- Wu, S. T., and W. P. Guo. A self-consistent numerical magnetohydrodynamic (MHD) model of helmet streamer and flux-rope interactions: Initiation and propagation of coronal mass ejections (CMEs), in *Coronal Mass Ejections, Geophys. Monogr. Ser.*, edited by N. Crooker, J. A. Joselyn, and J. Feynman, **99**, 83. AGU, Washington, 1997.

J. A. Linker, R. Lionello, and Z. Mikić, Science Applications International Corporation, 10260 Campus Point Drive, MS W2M, San Diego, CA 92121. (email: linker@iris023.saic.com; lionel@iris023.saic.com; mikic@iris023.saic.com)

T. Amari, Centre de Physique Théorique, École Polytechnique, 91128 Palaiseau Cedex, France (email: amari@cph.t.polytechnique.fr)

Received _____

¹Science Applications International Corporation, San Diego, California.

²Centre de Physique Théorique, École Polytechnique, France

Submitted to the *Journal of Geophysical Research*, 2000.

Figure 1. Simulated eruption of a magnetic flux rope on the Sun. (a) A three-dimensional flux rope formed by reducing the magnetic flux in a sheared arcade, computed with the polytropic model (see text). The flux rope lies within a helmet streamer that is surrounded by open magnetic field lines along which the solar wind streams outward. When the amount of magnetic flux decrease is small enough, the flux rope is stable. (b)-(d) Further reduction of the photospheric magnetic field leads to the eruption of the flux rope.

Figure 2. The evolution of the plasma density and magnetic field in a thermodynamic MHD model(see text). The plasma density is depicted in color, and projections of the magnetic field lines are overlaid on the density. (Corresponding plots of the temperature can be seen in Figure 3.) A closeup of the lower part of the simulation domain near the equator is shown. (a) The helmet streamer configuration at the end of the shearing phase. (b) The streamer after the magnetic flux has been reduced (reduction of 3.75% of the initial interior bipole). A low-lying filament structure has formed and is just discernible near the lower boundary (see Figure 4 for a zoomed view). (c) The filament is now at a height of 140,000 km and is moving upward slowly. The enhanced density can be seen to lie near the bottom of the detached flux surfaces. Flux reduction (at 11.25%) is beyond the critical threshold for eruption (see text). (d) the eruptive phase has started, and dense material is carried upward into the corona, shown in (e) and (f).

Figure 3. The same as Figure 2, except that the evolution of the plasma temperature and magnetic field are depicted. The high density material shown in Figure 2 is also very cold.

Figure 4. A zoomed view of the of the prominence-like structure when flux reduction is halted at a level of 3.75% ($t = 608\tau_A$, Figures 2b and 3b) and the calculation is continued (see text), allowing a stable flux rope to form. The plasma density (a) and temperature (b) are shown together with projections of the magnetic field lines as in Figures 2-3. Tracings of the magnetic field lines, colored by temperature (c) and density (d) are shown. The helical field lines support cold ($T \sim 2 \times 10^4 K$) and dense ($n \sim 10^{10}$) material against gravity.

Figure 5. The prominence height as function of time for the eruptive phase of the calculation (frames b-f of Figures 2-3).

Eruption of a 3D Flux Rope

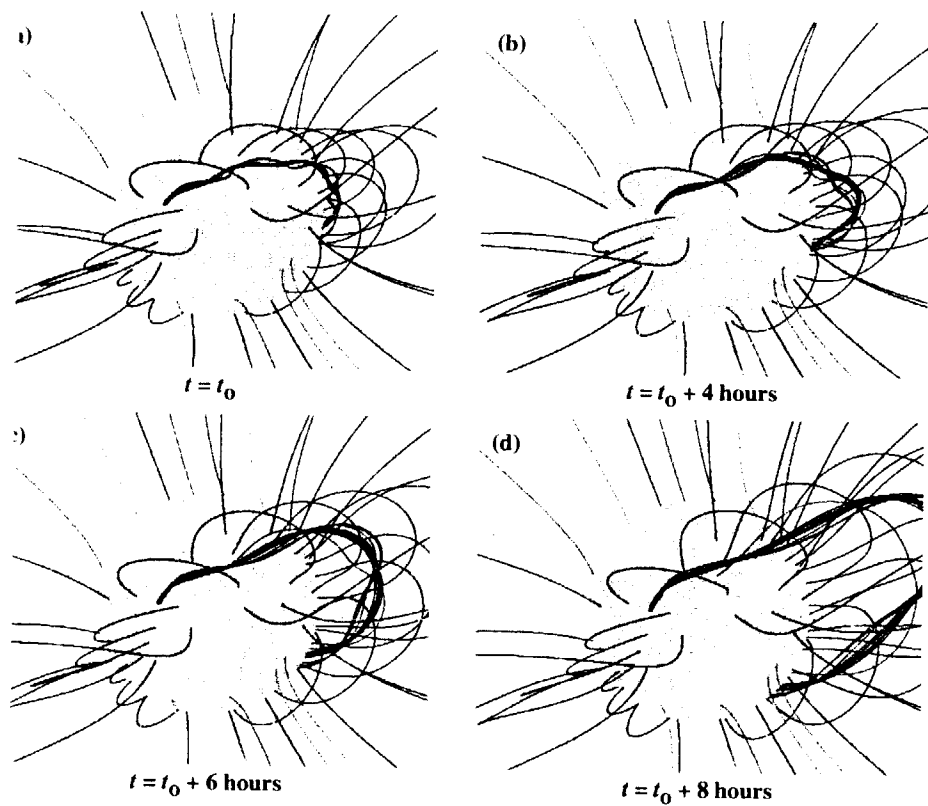


Figure 1

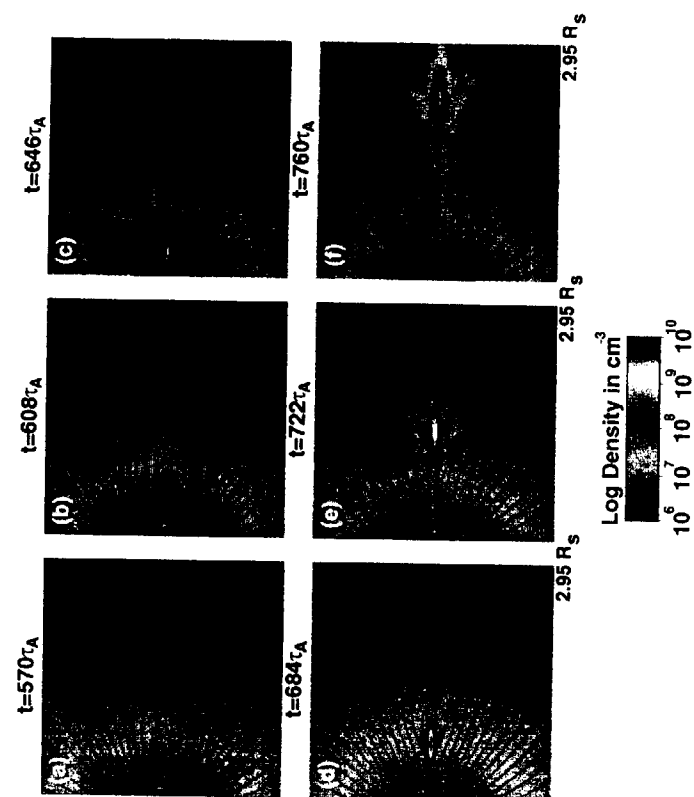


Figure 2

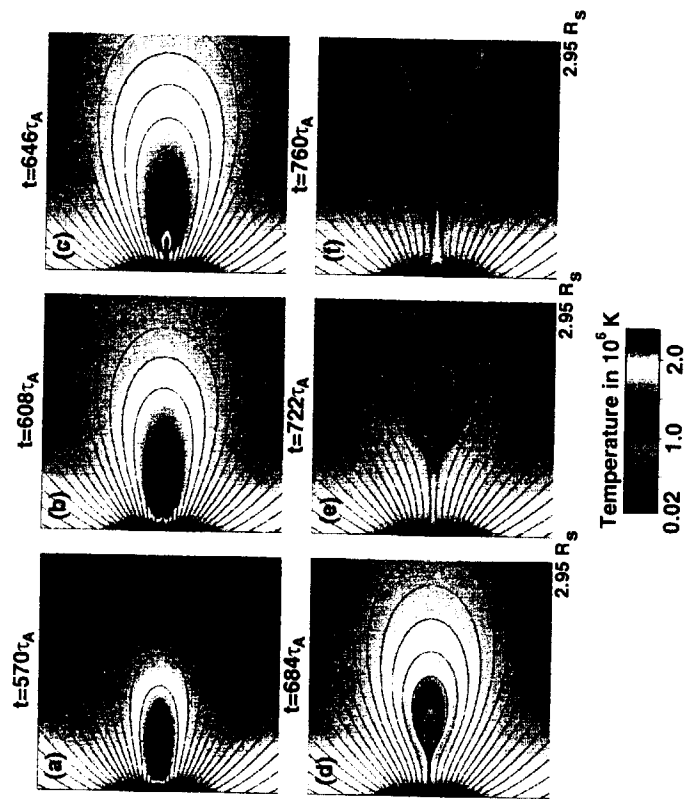


Figure 3

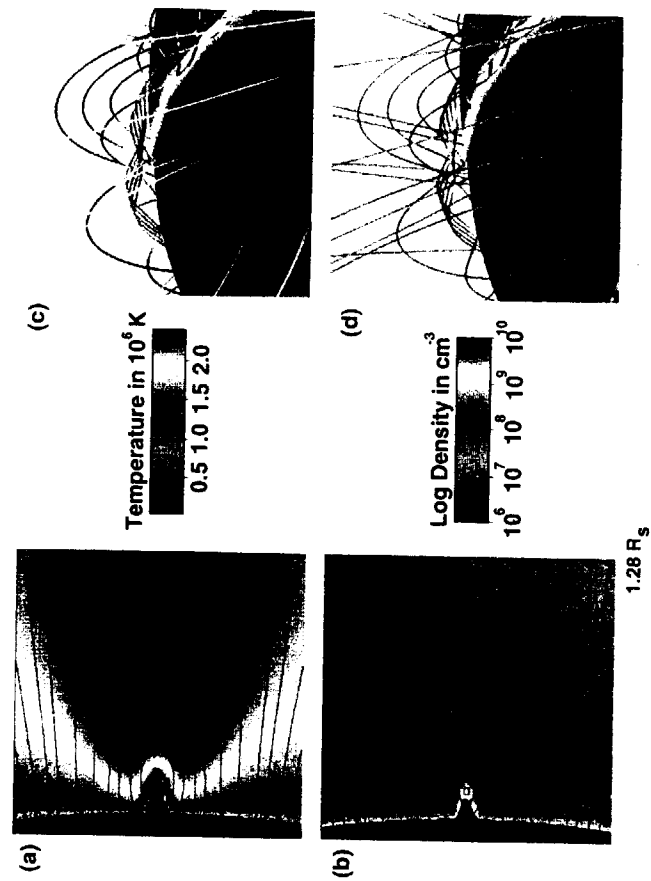


Figure 4

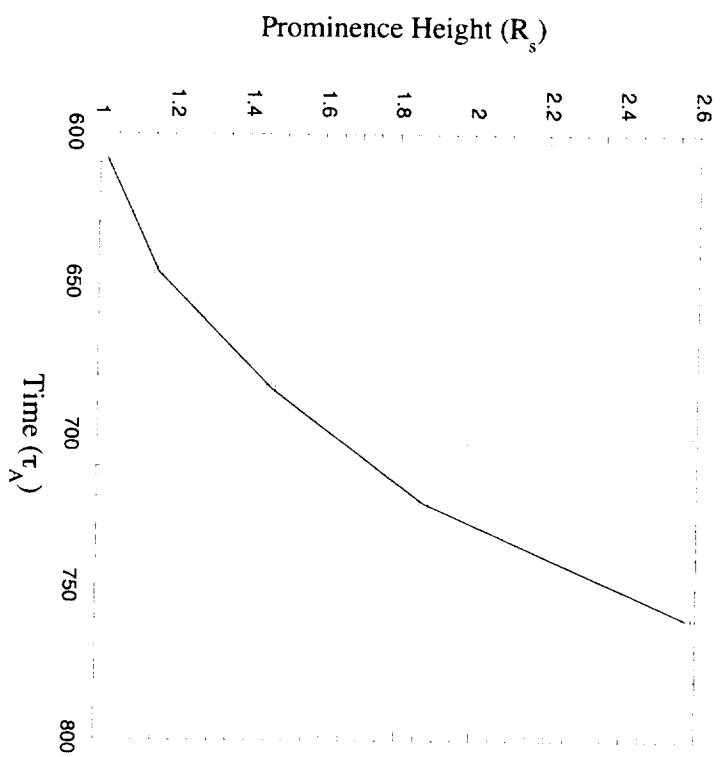


Figure 5